Complex aneuploidy triggers autophagy and p53-mediated apoptosis and impairs the second lineage segregation in human preimplantation embryos

Marius Regin[1], Yingnan Lei[1], Edouard Couvreu De Deckersberg[1], Yves Guns[2], Pieter Verdyck[3], Greta Verheyen[2], Hilde Van de Velde[2,4], Karen Sermon[1,#], Claudia Spits[1,#,*]

[1]Research Group Reproduction and Genetics, Faculty of Medicine and Pharmacy, Vrije Universiteit Brussel, Laarbeeklaan 103, 1090 Jette, Brussels, Belgium

[2]Brussels IVF, Universitair Ziekenhuis Brussel, Laarbeeklaan 101, 1090 Jette, Brussels, Belgium

[3]Vrije Universiteit Brussel (VUB), Universitair Ziekenhuis Brussel (UZ Brussel), Clinical Sciences, Research Group Reproduction and Genetics, Centre for Medical Genetics, Brussels, Belgium

[4]Research Group Reproduction and Immunology, Faculty of Medicine and Pharmacy, Vrije Universiteit Brussels, Laarbeeklaan 103, 1090 Jette, Brussels, Belgium

[#]These authors contributed equally to this work.

*Corresponding author: Claudia.Spits@vub.be

Abstract

About 70% of human cleavage stage embryos show chromosomal mosaicism, falling to 20% in blastocysts. Chromosomally mosaic human blastocysts can implant and lead to healthy new-borns with normal karyotypes. Studies in mouse embryos and human gastruloids have shown that aneuploid cells show proteotoxic stress, autophagy and p53 activation and that they are eliminated from the epiblast by apoptosis while being rather tolerated in the trophectoderm. These observations suggest a selective loss of aneuploid cells from human embryos, but the underlying mechanisms are not yet fully understood. In this study we investigated the cellular consequences of aneuploidy in a total of 85 human blastocysts. RNA-sequencing of trophectoderm cells showed transcriptional signatures of a deregulated p53 pathway and apoptosis, which was proportionate to the level of chromosomal imbalance. Immunostaining revealed that aneuploidy triggers proteotoxic stress, autophagy and apoptosis in aneuploid embryos. Total cell numbers were lower in aneuploid embryos, due to a decline both in trophectoderm and in epiblast/primitive endoderm cell numbers. While lower cell numbers in trophectoderm may be attributed to apoptosis, it appeared that aneuploidy impairs the second lineage segregation and primitive endoderm formation in particular. Our findings might explain why fully aneuploid embryos fail to further develop and we hypothesize that the same mechanisms lead to removal of aneuploid cells from mosaic embryos. This hypothesis needs further study as we did not analyse chromosomal mosaic embryos. Finally, we demonstrated clear differences with previous findings in the mouse, emphasizing the need for human embryo research to understand the consequences of aneuploidy.

Introduction

Aneuploidy is common in human preimplantation embryos from both natural (Munné *et al.*, 2020a) and medically assisted reproduction cycles (Voullaire *et al.*, 2000; Wells and Delhanty, 2000; Vanneste *et al.*, 2009; Johnson *et al.*, 2010; Chavez *et al.*, 2012; Mertzanidou *et al.*, 2013b, 2013a; Chow *et al.*, 2014; Fragouli *et al.*, 2019; Popovic *et al.*, 2020; Starostik *et al.*, 2020; Capalbo *et al.*, 2021; Yang *et al.*, 2021). Depending on the study, up to 80% of human cleavage stage embryos are found to be aneuploid, of which 70% show chromosomal mosaicism, i.e. the presence of at least two cell lineages with different genomic content (Regin *et al.*, 2022). The reasons behind this high rate of chromosomal abnormalities of mitotic origin is still largely unknown (McCoy, 2017) but could be a combination of a weak spindle assembly checkpoint (SAC) that is uncoupled of apoptosis until the blastocyst stage (Jacobs *et al.*, 2017; Vázquez-Diez *et al.*, 2019), in combination with an abundancy of transcripts of anti-apoptotic genes in cleavage-stage embryos (Yan *et al.*, 2013). After embryonic genome activation, the rapidly increasing expression of pro-apoptotic genes along with the full functionality of the SAC establishes the control of mitotic errors.

It is by now well established that chromosomally mosaic embryos can result in healthy new-borns with normal karyotypes, implying a progressive and selective loss of aneuploid cells during development (Greco *et al.*, 2015; Fragouli *et al.*, 2017, 2019; Munné *et al.*, 2017, 2020b; Capalbo *et al.*, 2021; Viotti *et al.*, 2021; Yang *et al.*, 2021). In the preimplantation embryo, several studies have shown that the proportion of aneuploid cells within the embryo decreases three days post fertilization (3dpf) (van Echten-Arends *et al.*, 2011; Fragouli *et al.*, 2019; Yang *et al.*, 2021) with no apparent preferential allocation of aneuploid cells during the first lineage segregation event to either trophectoderm (TE) or inner cell mass (ICM) (Capalbo *et al.*, 2013; Popovic *et*

71 *al.*, 2018; Starostik *et al.*, 2020; Ren *et al.*, 2022). However, aneuploid cells can be
72 excluded as cell debris (Orvieto *et al.*, 2020) or allocated to the blastocoel cavity and
73 to peripheral cells that do not participate in the formation of the embryo (Griffin *et al.*,
74 2022). In some studies, (Starostik *et al.*, 2020; Griffin *et al.*, 2022) the TE contained a
75 slightly higher number of aneuploid cells than the ICM, without reaching statistical
76 significance. In their landmark paper, (Bolton *et al.*, 2016) found a quite similar but
77 statistically significant 6% TE enrichment in mouse embryos treated with the SAC
78 inhibitor reversine to induce mosaic aneuploidy. This small enrichment fell in the same
79 confidence interval as the Starostik study, therefore TE enrichment cannot be ruled out
80 in the human embryo. After implantation, aneuploid cells become progressively more
81 frequent in the trophoblast lineage which is derived from TE cells as compared to the
82 epiblast (EPI) and primitive endoderm (PrE) lineages which are derived from the ICM
83 cells during the second lineage segregation (Starostik *et al.*, 2020). This suggests that
84 the trophoblast cells are more tolerant to aneuploidy, in line with the rate of 1-2% of
85 confined placental mosaicism observed in ongoing pregnancies in the general
86 population (Kalousek and Vekemans, 1996) and with the presence of aneuploid cells
87 in the placental lineages only (Zamani Esteki et al., 2019). This is further supported by
88 a recent study showing that genetic mosaicism is a normal feature of the placenta and
89 is due to genetic bottlenecks that occur early in development (Coorens *et al.*, 2021).
90 Taken together, strong evidence supports the selective elimination of aneuploid cells
91 from the embryonic lineage in the pre- and post-implantation development, while the
92 placenta appears to be more tolerant to genetic imbalances.

93 From a cellular point of view, aneuploidy has two types of consequences. Imbalances
94 of a specific chromosome, such as trisomy 21 or trisomy 18, can result in different
95 phenotypes, as evidenced by the human Down and Edwards syndromes. These

96 imbalances can manifest early on during early embryo development (Licciardi *et al.*,
97 2018; Fuchs Weizman *et al.*, 2019; Sanchez-Ribas *et al.*, 2019; Shahbazi *et al.*, 2020).
98 Moreover, aneuploidy as such also elicits two highly conserved intracellular stress
99 responses, that have been found from yeast and plants to mouse and human cells
100 (reviewed in: Santaguida and Amon, 2015; Zhu et al., 2018; Chunduri and Storchová,
101 2019; Chunduri et al., 2022; Krivega et al., 2022), and which are likely at the basis of
102 the selective clearance of aneuploid cells during development. First, aneuploidy results
103 in gene-dosage defects, leading to an unbalanced protein pool and proteotoxic stress
104 (Torres *et al.*, 2007; Huettel *et al.*, 2008; Williams *et al.*, 2008; Tang *et al.*, 2011;
105 Oromendia *et al.*, 2012; Stingele *et al.*, 2012; Donnelly *et al.*, 2014; Ohashi *et al.*, 2015).
106 If this remains unresolved by activation of autophagy (Stingele *et al.*, 2012; Dürrbaum
107 *et al.*, 2014; Santaguida *et al.*, 2015; Ariyoshi *et al.*, 2016), CASP8/LC3B/p62 may
108 interact to activate the apoptosis cascade (Pan *et al.*, 2011). Second, aneuploidy
109 results in replication stress that can lead to DNA-damage, resulting in *p53* activation
110 (Li *et al.*, 2010; Thompson and Compton, 2010; Santaguida *et al.*, 2017) and ultimately
111 to cell cycle arrest and apoptosis (reviewed in: Santaguida and Amon, 2015; Zhu et
112 al., 2018; Regin et al., 2022).

113 During early embryo development of the mouse, Bolton *et al*. (Bolton *et al.*, 2016)
114 showed that aneuploid cells are selectively cleared from chimeric embryos generated
115 from control blastomeres mixed with aneuploid blastomeres obtained using a
116 treatment with the SAC inhibitor reversine. Later work by the same group showed that
117 apoptosis of these aneuploid cells requires autophagy and *p53* activation and that
118 euploid cells in the mouse embryo compensate this cell loss by increased proliferation
119 (Singla *et al.*, 2020). The authors proposed that the proteotoxic stress in these
120 aneuploid chimeric mouse embryos activated the p53 pathway, which in turn activated

121 autophagy and apoptosis. In a recent study using human 2D gastruloids with reversine-
122 induced aneuploidy, apoptosis was only induced in differentiating but not in pluripotent
123 cells, although aneuploidy induced an increase in total nuclear p53 proteins (Yang *et*
124 *al.*, 2021). The apoptotic response to aneuploidy also seems to be lineage-specific. In
125 the mouse, aneuploid cells in the ICM are eliminated by apoptosis while they are rather
126 tolerated in the TE (Bolton *et al.*, 2016). Furthermore, in a follow-up study, (Singla *et*
127 *al.*, 2020) demonstrated that during the peri-implantation period, aneuploid cells were
128 eliminated from the EPI and the PrE at similar rates, and that the EPI-specific
129 elimination of aneuploid cells by apoptosis is coupled to increased proliferation rates
130 of euploid cells. Similarly, in human gastruloids, aneuploid cells are eliminated by
131 apoptosis from the embryonic germ layers but are tolerated in the TE-like cells (Yang
132 *et al.*, 2021).

133 The type of aneuploidy and the percentage of aneuploid cells within a
134 euploid/aneuploid mosaic embryo determine its developmental capacity. The viability
135 of mouse embryos inversely correlates to the proportion of aneuploid cells, with 50%
136 of euploid cells being sufficient to sustain normal development (Bolton *et al.*, 2016).
137 This same threshold appears to apply to human embryos, where embryos with less
138 than 50% of aneuploid cells have higher developmental potential than those containing
139 more than 50%, albeit both performing worse than fully euploid embryos (Viotti et al.,
140 2021, Capalbo et al., 2021). Conversely, whole chromosome gains and losses that are
141 present in every cell of the human embryo are usually linked to lethality with the notable
142 exception of trisomies 13 (Patau syndrome), 18 (Edwards syndrome) and 21 (Down
143 syndrome), and sex chromosome abnormalities. Shahbazi *et al*. recently described the
144 consequences of carrying specific meiotic aneuploidies on human embryo
145 development using an *in vitro* implantation model (Shahbazi *et al.*, 2020). They showed

146 that human embryos with trisomy 15, 16 and 21 and monosomy 21 readily all reached
147 the blastocyst stage, and that monosomy 21 embryos arrested after implantation while
148 trisomy 15 and 21 embryos developed further. Interestingly, trisomy 16 embryos
149 showed a hypoproliferative trophoblast due to excessive *CDH1* expression, a gene
150 located on chromosome 16.

151 In this study, we investigated the cellular responses to complex aneuploidy during
152 human preimplantation development, with a focus on stress response and lineage
153 segregation events.

154 **Methods**

155 **Ethical approval.** All experiments have been approved by the local Commission of
156 Medical Ethics of the UZ Brussel (B.U.N. 143201628722) and the Federal Committee
157 for Medical and Scientific Research on Human Embryos *in vitro* (AdV069 and AdV091).
158 Patients from Brussels IVF (UZ Brussel) donated their embryos for research after
159 written informed consent.

160 **Culture of human pre-implantation embryos.** We warmed vitrified human
161 blastocysts (5-6dpf) after PGT or at 3dpf using the Vitrification Thaw Kit (Vit Kit-Thaw;
162 Irvine Scientific, USA) following manufacturer's instructions. Embryos were graded
163 before vitrification by experienced clinical embryologists according to Gardner and
164 Schoolcraft criteria (Gardner and Schoolcraft, 1999). Post PGT-embryos were left to
165 recover for 2h in 25 µL droplets of Origio Sequential Blast™ medium (Origio) at 37°C
166 with 5% O_2, 6% CO_2 and 89% N_2, after which they underwent a second TE biopsy (Fig.
167 1a). For the reversine experiment, we cultured the 3dpf embryos for 24h in the same
168 medium supplemented with 0.5 µM reversine (Stem Cell Technologies) and after
169 wash-out we let them develop until 5dpf and subsequently took a biopsy (Fig. 1b). The
170 PGT embryos (5dpf or 6dpf) used for the second experiment series (Fig. 4a) were
171 cultured for 16h after warming to ensure sufficient time to progress to the second
172 lineage differentiation. Prior to fixation we live-stained all the embryos with either
173 Caspase-3/7 or Caspase-8 (Supplementary Table 30) for 30 min and subsequently
174 removed the zona pellucida using Acidic Tyrode's Solution (Sigma-Aldrich) for 30 sec
175 – 2 min and subsequently washed in PBS/2%BSA.

176 **Biopsy procedure.** The zona pellucida was opened (15-25µm) on 4dpf using a Saturn
177 Laser (Cooper Surgical). For PGT cycles, expanded good quality embryos were

178 biopsied on 5dpf; early blastocysts were evaluated again for expansion on 6dpf. Briefly,
179 embryos were transferred to HEPES buffered medium and biopsied on a Nikon
180 inversed microscope equipped with a Saturn Laser. The herniated TE cells were then
181 aspirated and cut using manual laser shoots. In case of sticking cells this was
182 supported by mechanical cutting. After successful tubing, the blastocysts were vitrified
183 using CBS-VIT High-Security straws (CryoBioSystem, L'Aigle, France) with
184 dimethylsulphoxide-ethylene glycol-sucrose as the cryoprotectants (Irvine Scientific
185 Freeze Kit, Newtownmountkennedy, County Wicklow, Ireland) (Van Landuyt *et al.*,
186 2011). The TE biopsy for RNA-sequencing (Fig. 1a,b) was performed with the same
187 procedure, cells were biopsied form the same opening in the zona pellucida.

188 **PGT.** During PGT we analyzed a TE sample with multiple cells for each embryo. Next
189 Generation Sequencing: The chromosomal analysis was performed by WGA
190 (Sureplex, Illumina) followed by library preparation (KAPA HyperPlus, Roche),
191 sequencing on a NovaSeq (Illumina) and an *in-house* developed interpretation
192 pipeline. The analysis has an effective resolution of 5 Mb.

193 SNP-array: We relied on whole genome amplification (MDA, Repli-G) followed by
194 genome wide SNP array using Karyomapping (Vitrolife) with Bluefuse software
195 (Vitrolife). In addition, SNP array data were analyzed with an *in-house* developed
196 interpretation pipeline for aneuploidy detection.

197 **RNA-sequencing.** Multiple (5-10) TE cells were used as input to generate full length
198 cDNA with the SMART-Seq™ v4 Ultra™ Low Input RNA Kit (Clontech Laboratories,
199 Inc.) according to the manufacturer's instructions. The quality of cDNA was checked
200 using the AATI Fragment Analyzer (Advances Analytical). Library preparation was
201 performed using the KAPA HyperPlus Library Preparation Kit (KAPA Biosystems)

202 according to the manufacturer's instructions. During cDNA synthesis and library
203 preparation we used 17 and 11 PCR cycles, respectively. Sequencing was performed
204 on a NovaSeq 6000 (Illumina) with 25 million reads per sample.

205 **Bioinformatics analysis.** Reads were trimmed using cutadapt version 1.11 to remove
206 the "QuantSEQ FWD" adaptor sequence. We checked the quality of the reads using
207 the FastQC algorithm (Love *et al.*, 2014). Count tables were generated using STAR
208 (Dobin *et al.*, 2013) (version 2.5.3) through mapping against the Genome Reference
209 Consortium Human Build 38 patch release 10 (GRCh38.p10) combined with a general
210 transfer format (GTF) file, both downloaded from the Ensembl database. The RNA-
211 sequencing by Expectation Maximization (RSEM) (Li and Dewey, 2011) software
212 (version 1.3.0) was used to produce the count tables.

213 Differential gene expression analysis was performed using R-studio (Version 1.1.456)
214 with the edgeR (Robinson *et al.*, 2009) and limma (Ritchie *et al.*, 2015) packages. We
215 included genes with a count per million greater than 1 in at least two samples. The
216 trimmed mean of M values (Robinson and Oshlack, 2010) algorithm was used for
217 normalization. The normalized counts were then transformed in a $\log_2$ fold-change
218 ($\log_2$FC) table with their associated statistics. In each comparison, genes with a |
219 $\log_2$FC | > 1 and an p-value < 0.05 were considered as significantly differentially
220 expressed.

221 Gene set enrichment analysis (GSEA) was performed using the 'investigate gene sets'
222 function on the website of the Molecular Signature Database (http://www.gsea-
223 msigdb.org/gsea/msigdb/annotate.jsp). We used all differentially expressed genes
224 (Supplementary Tables 2, 3) as input and investigated Hallmark, C2 and C5 gene sets
225 with FDR-q values < 0.05. For the analysis of gene dosage effects, we could only use

226 the TOP500 differentially expressed genes by p-value since the Molecular Signature
227 Database changed the cut-off during the period of our data analysis (raw data,
228 Supplementary Tables 26, 27). In the figures 1f and g we used a supervised approach
229 and sorted the significantly deregulated gene sets by the total amount of genes in
230 overlap. Figure 2f was also supervised but the gene sets were sorted by FDR-q value.

231 Ingenuity Pathway analysis (IPA, Qiagen Inc.) was used to investigate activated,
232 deregulated and inhibited upstream regulators and canonical pathways. As for the
233 GSEA we used all differentially expressed genes of our two test sets with their
234 respective $\log_2$FC and p-value. For the upstream regulators IPA computes z-scores
235 with associated p-values that are considered significant when $p < 0.05$. If significant, a
236 z-score > 2 means activated, a z-score < 2 means inhibited and in between means
237 deregulated. For the canonical pathways IPA computes z-scores with associated p-
238 values that are considered significant when $p < 0.05$. If significant, we considered a z-
239 score > 1.5 as activated, a z-score < 1.5 as inhibited and in between as deregulated.
240 We generated all figures in a supervised approach.

241 Transcription factor analysis of all differentially expressed genes was performed using
242 Enrichr (https://maayanlab.cloud/Enrichr/). We selected the outputs from ChEA 2016
243 and ENCODE ChEA consensus and considered those transcription factors as
244 significant with a p-value < 0.05.

245 The copy number variation (CNV) analysis was inferred from our RNA-sequencing
246 data set using *inferCNV* R package (version 1.7.1) (Inferring copy number alterations
247 from tumor single cell RNA-Seq data
248 (https://github.com/broadinstitute/inferCNV/wiki"). Our count table was used as input
249 and compared to the reference set which in our case was the expression data of the

250 euploid embryos. The analysis followed the standard workflow in inferCNV with the
251 following parameters: “denoise” mode, value of 1 was used for the “cutoff”, prediction
252 of CNV states using default Hidden Markov Models (HMM) method,
253 “cluster_by_groups” was set to TRUE, and other values were set by default.

254 All figures were generated using R-studio (Version 1.1.456).

255 **Gene dosage analysis.** We calculated the total number of loci with imbalanced gene
256 expression based on the genetic abnormalities identified during the PGT. For this, we
257 used the number of coding loci per chromosomal region as listed in the ENSMBL
258 database (ensemble.org) and included both gains and losses, either mosaic or
259 homogeneously present, and both full chromosomal aneuploidy as well as segmental
260 abnormalities. The embryos were ranked based on the total number of imbalanced loci
261 and separated into a low- and a high-imbalanced gene dosage group. The low-dosage
262 group contained the embryos with the lowest 50th percentile in number of unbalanced
263 loci, the high-dosage group the embryos with 50th percentile or higher (Supplementary
264 Table 25, 29).

265 **Immunocytochemistry.** Embryos were fixed using 4% paraformaldehyde (Sigma-
266 Aldrich) for 10 min, washed three times in PBS/2%BSA for 5 min and then
267 permeabilized using 0.1% Triton X-100 (Sigma-Aldrich) for 20 min followed by another
268 washing cycle. We used 10% FBS supplemented with 2% BSA for 1h to block non-
269 specific protein binding. The embryos were then incubated overnight with primary
270 antibodies (Supplementary Table 30) diluted in blocking buffer at 4°C. The next day,
271 they underwent another washing cycle using PBS/2%BSA and were then incubated
272 with secondary antibodies (1:200, Supplementary Table 26) for 1h at room
273 temperature. After washing, nuclei were stained using Hoechst 33342 (5µg/mL, Life

274 Technologies) diluted in PBS/2%BSA for 15 min. For imaging we mounted the
275 embryos on poly-L-lysine coated glass slides (Sigma-Aldrich) in 3µL of PBS. To avoid
276 flattening of the embryos we used Secure-Seal^{TM} Spacers (9mm diameter, 0.12mm
277 deep, Thermofisher) before putting the coverslips in place. For the experiments that
278 required re-staining (Fig. 4a) we imaged the embryos in 3µL PBS/2%BSA in 18 well µ-
279 Slides (Ibidi) and subsequently recuperated them. After recuperation we
280 photobleached the embryos stained for CASP3/7 by using maximum laser power of
281 the 488 nm channel and maximum size of the pinhole for 10 min. The embryos were
282 then re-stained using rat-anti-GATA4 primary antibody and the matching Alexa Fluor
283 488 secondary antibody (Supplementary Table 30) (to replace the CASP3/7 staining).

284 **Imaging and image analysis.** Confocal imaging was performed using the LSM800
285 (Zeiss). Z-stacks were taken with a LD C-Apochromat 40x/1.1 NA water immersion
286 objective in optical sections of 1µm. Nuclei were counted using Arivis Vision 4D (3.4.0).
287 All other measurements were performed using the Zen 2 (blue edition) software based
288 on the optical sections and/or orthogonal projections.

289 **Statistics.** The type of statistical test and p-values are mentioned in the figure legends.
290 For experiments that contained groups with small sample sizes we used non-
291 parametric tests (Mann-Whitney or Kruskal-Wallis test). Fisher-exact test was used to
292 determine the dependency of the ploidy status on the presence or absence of primitive
293 endoderm and to test for differences in the quality of the ICM of euploid and aneuploid
294 embryos. Otherwise we used Student's t-test with Welch's correction when we
295 assumed normal distribution and unequal standard deviations. We used GraphPad
296 Prism 9.0.0 or R-studio for statistical testing. The trend analysis regarding gene dosage
297 effects was performed with SPSS using the Jonkheere-Terpstra test.

298 **Results**

299 **Human embryos with meiotic complex aneuploidy show transcriptional**
300 **signatures of a deregulated p53 pathway and apoptosis**

301 We first tested the hypothesis that chromosomally unbalanced cells are cleared during
302 human preimplantation development by apoptosis, mediated by both sustained p62-
303 LC3B accumulation as a marker for autophagy and DNA-damage-mediated p53
304 activation. Fifty cryopreserved human blastocysts (5 or 6dpf) that had been previously
305 diagnosed by Preimplantation Genetic Testing (PGT) as either euploid (n=28) or
306 containing non-mosaic complex aneuploidy of at least two whole chromosomes and
307 assumed of meiotic origin (except for one) (n=22, further referred to as aneuploid, Fig.
308 1a, Supplementary Table 1) underwent a second TE biopsy to collect cells for RNA
309 sequencing. Eleven warmed human cleavage stage embryos that were treated with
310 0.5 μM reversine from 3dpf to 4dpf and further developed to the blastocyst stage
311 (referred to as reversine-treated embryos, Fig. 1b) were also biopsied on 5dpf to serve
312 as a comparison with the results obtained in the mouse. The concentration of 0.5 μM
313 reversine was chosen based on previous experiments in mouse embryos (Bolton *et*
314 *al.*, 2016; Singla *et al.*, 2020). Of these, 14 euploid, 20 aneuploid and 11 reversine-
315 treated embryos (total=45) yielded good quality RNA-sequencing results.

316 Unsupervised hierarchical clustering and principal component analysis using all
317 expressed genes revealed no clustering of the euploid, aneuploid or reversine-treated
318 embryos in distinct groups (Fig. 1c, Supplementary Fig. 1a). We used InferCNV
319 (https://github.com/broadinstitute/inferCNV/wiki") to bioinformatically infer unbalanced
320 chromosomal copy numbers from gene expression data, based on higher or lower
321 expression of genes located on chromosomes with gains or losses respectively (Fig.

322 1d, Supplementary Fig. 1b, Supplementary Table 1). We compared the outcomes to
323 the results obtained during PGT and found a match for 45/48 of the full chromosome
324 aneuploidies, while euploidy was correctly predicted in all cases (Supplementary Fig.
325 1b). These results show that aneuploidy in human blastocysts results in significant
326 abnormal gene dosage effects. The exact karyotypes of the reversine-treated embryos
327 could not be determined since reversine induces different aneuploidies in each cell,
328 leading to mosaic TE biopsies. However, InferCNV allowed us to determine a trisomy
329 12 meiotic chromosomal abnormality in one reversine-treated embryo (Supplementary
330 Figure 1c), confirming that the reversine treatment causes random aneuploidy while
331 naturally occurring meiotic aneuploidies are readily determined.

332 Despite the abnormal gene dosage, and in line with the lack of clear clustering in the
333 PCA, the differential gene expression analysis yielded very few genes with a false
334 discovery rate (FDR-q-value) under 0.05. These findings are similar to those of other
335 studies on the transcriptome of aneuploid human embryos (Groff *et al.*, 2019; Maxwell
336 *et al.*, 2022). Therefore, we used the differential gene expression with a cut-off value
337 of $|\log_2$ fold change$|>1$ and $-\log_{10}$(p-value)<0.05, and primarily focused on pathway
338 analysis. We found 547 upregulated and 463 downregulated genes in aneuploid
339 versus euploid embryos (Fig. 1e, Supplementary Table 2). Amongst the top
340 upregulated genes was Growth Differentiation Factor 15 (*GDF15*), a gene that has
341 been found to be upregulated in human aneuploid cells (Dürrbaum *et al.*, 2014)
342 including aneuploid human embryos (Starostik *et al.*, 2020). When comparing
343 reversine-treated versus euploid embryos we observed 539 upregulated and 355
344 downregulated genes (Fig. 1f, Supplementary Table 3). While only 9.6% of the
345 differentially expressed genes are in common between the aneuploid and reversine-
346 treated embryos (Fig. 1g, h, Supplementary Table 4), pathway analysis revealed

347 several commonly deregulated pathways. We identified deregulation of the p53
348 pathway and apoptosis (FDR q-value < 0.05, Fig. 1i, Supplementary Tables 5, 6) and
349 deregulation of cell population proliferation, apoptotic process, regulation of cell death,
350 and cell cycle (Fig. 1j, Supplementary Tables 7, 8). The prediction of p53 activation is
351 also supported by differential expression of several p53 target genes (Jaiswal *et al.*,
352 2021), such as *MDM2* and *PPM1D* (feedback); *CDKN1A, BTG2, GADD45A* (cell-cycle
353 arrest); *TNFRSF10B* (apoptosis), *DDB2* and *RRM2B* (DNA-repair); *FDXR*
354 (metabolism) and *SESN1* (translation control) (Supplementary Table 2). Other
355 pathways of interest related to DNA damage and p53, such as cellular response to
356 DNA damage stimulus and DNA damage response signal transduction by p53 class
357 mediator were specific to the aneuploid group. Cellular senescence signatures in the
358 aneuploid embryos and selective autophagy in the reversine-treated group were also
359 deregulated (Supplementary Tables 9, 10). Ingenuity pathway analysis (IPA) showed
360 that upstream regulators *CDK19* and *AURK* (cell cycle) and *GAS2L3* and *ANLN* (cell
361 growth) were inhibited in the aneuploid group (Fig. 1k, Supplementary Table 11). In
362 line with the GSEA analysis, *p53* was the most activated upstream regulator.
363 Reversine-treated embryos activated *ATM* which is a well-known sensor of DNA-
364 damage that mediates target genes such as *p53* (Banin *et al.*, 1998) (Fig. 1l,
365 Supplementary Table 12). Canonical pathway analysis by IPA confirmed that p53
366 signalling, autophagy, cell-cycle pathways and senescence are deregulated in
367 aneuploid embryos (Fig. 1m, Supplementary Table 13). The TE of reversine-treated
368 embryos showed activated senescence, similar to the mouse reversine-treated
369 embryos (Bolton *et al.*, 2016) (Fig. 1n, Supplementary Table 14). Transcription factor
370 analysis identified significant *p53* expression in both aneuploid and reversine-treated
371 groups (Supplementary Tables 15, 16).

372 We next compared our set of differentially expressed genes to those identified by other
373 studies investigating the gene expression of euploid and aneuploid embryos, namely:
374 mosaic monosomies 4, 7, 10, 15, 19 and mosaic trisomies 15 and 19 (Maxwell *et al.*,
375 2022), trisomy 16 and monosomy 16 (Fuchs Weizman *et al.*, 2019), monosomy 21
376 (Sanchez-Ribas *et al.*, 2019) and embryos that contained various types of
377 chromosomal abnormalities (Vera-Rodriguez *et al.*, 2015; Licciardi *et al.*, 2018;
378 Starostik *et al.*, 2020; Martin *et al.*, 2023) (detailed overview in Supplementary Table
379 17). Overall, we found modest overlaps (Supplementary Figure 1d,e, Supplementary
380 Tables 18-20). Most commonalities were with the data of Starostik et al, where we
381 found an overlap in 87 genes (2.3%) (Starostik *et al.*, 2020). These included target
382 genes of the p53 pathway such as *MDM2* and *CDKN1A* (Supplementary Fig. 1d,
383 Supplementary Table 20). Interestingly, GSEA of these 87 genes identified an
384 enrichment of intrinsic apoptotic signalling pathway by p53 class mediator and the
385 apoptotic signalling pathway, in line with the findings of our dataset (Supplementary
386 Table 19).

387 **High gene-dosage imbalances result in stronger cellular stress signatures in**
388 **human embryos**

389 To test if there was a relationship between the level of stress signatures and the size
390 of chromosomal imbalances in embryos as previously described in cancer (Dürrbaum
391 and Storchová, 2016), we separated the aneuploid group into a low- and a high-
392 imbalanced gene dosage group, based on the total number of coding loci that were
393 affected by the chromosomal abnormalities. The low-dosage group contained the
394 embryos under the 50th percentile when ranking the embryos from the lowest to the
395 highest number of unbalanced loci, the high-dosage group the embryos with 50th
396 percentile or higher (Supplementary Table 21). Hierarchical clustering using the top

397 500 deregulated genes showed that all high-dosage embryos clustered together and
398 separated from the euploid embryos, while the low-dosage embryos clustered with
399 either group (Fig. 2a). Differential gene expression with $|\log_2$ fold change$|>1$ and -
400 $\log_{10}$(p-value)<0.05 resulted in 404 upregulated and 340 downregulated genes in low-
401 dosage versus euploid embryos and in 716 upregulated and 627 downregulated genes
402 in high-dosage versus euploid embryos with an overlap of 104 (10%) between both
403 aneuploid groups (Fig. 2b-e, Supplementary Tables 22,23). We identified deregulation
404 of TNFA signalling via NFkB, p53 pathway and apoptosis for both groups (FDR q-value
405 < 0.05, Fig. 2f, Supplementary Tables 24,25). High-dosage embryos additionally
406 showed an unfolded protein response, suggesting that this signature may only be
407 present in the embryos with more and/or larger abnormal chromosomes. In the high-
408 dosage group more of the genes of the p53 and apoptosis pathways were deregulated,
409 and with higher significance (Fig. 2g,h, Supplementary Tables 26,27). The gene
410 expression levels in the p53 and apoptosis pathways show a stepwise distribution
411 between the gene dosage groups (Fig. 2i).

412 **Aneuploidy triggers proteotoxic stress, autophagy and apoptosis in human**
413 **embryos**

414 To further investigate the cellular stress responses identified by the transcriptomic
415 analysis, we immunostained the same embryos that underwent TE biopsy for
416 transcriptome analysis. Thirty-seven (18 euploid, 19 aneuploid) of the 50 PGT embryos
417 and 8 of the 11 reversine-treated embryos were successfully stained for markers of
418 apoptosis, proteotoxic stress and autophagy (Fig. 3a,b). Aneuploid embryos showed
419 increased intensity levels of active CASP3/7 (13 euploid and 8 aneuploid embryos
420 stained) and CASP8 (6 euploid, 9 aneuploid and 8 reversine-treated embryos stained)
421 (Fig. 3c-f). Both aneuploid and reversine-treated embryos had lower cell numbers than

422 euploid embryos (Fig. 3g). We investigated whether proteotoxic stress and autophagy
423 (Oromendia *et al.*, 2012; Stingele *et al.*, 2012; Dürrbaum *et al.*, 2014; Ohashi *et al.*,
424 2015; Singla *et al.*, 2020) were also present in aneuploid human embryos. The number
425 of puncta per cell of autophagy markers LC3B (19 euploid, 22 aneuploid and 8
426 reversine-treated embryos stained) and p62 (6 euploid and 9 aneuploid embryos
427 stained) and the intensity levels of proteotoxic stress marker HSP70 (13 euploid, 8
428 aneuploid and 8 reversine-treated embryos stained) were significantly increased in
429 both aneuploid and reversine-treated embryos (Fig. 3h-k). The gene expression
430 profiles suggest that the accumulation of autophagic proteins in aneuploid embryos is
431 caused by increased autophagic flux due to differential expression of the *p53* target
432 gene DNA Damage Regulated Autophagy Modulator-1 (*DRAM1*), rather than by
433 inhibition of autophagy (Supplementary Table 2). DRAM1 is located in the lysosomal
434 membrane and it increases autophagic flux and apoptosis after stress-induced p53
435 activation in cancer cells (Crighton *et al.*, 2006; Guan *et al.*, 2015).

436 **Aneuploidy increases apoptosis in the trophectoderm and impairs the second**
437 **lineage segregation in the inner cell mass**

438 We further investigated if these effects are cell-type specific, as shown in the mouse
439 (Bolton *et al.*, 2016; Singla *et al.*, 2020) and human 2D gastruloids (Yang *et al.*, 2021),
440 and how they affect the first lineage segregation event to TE and ICM, and the second
441 lineage segregation event to EPI and PrE.

442 We co-stained a new batch of expanded blastocysts for OCT4 (10 euploid, 14
443 aneuploid, ICM/EPI) and CASP3/7 (10 euploid, 14 aneuploid), LC3B (4 euploid, 5
444 aneuploid) or Serine 15 p53 (3 euploid, 5 aneuploid) (Fig. 4a). To ensure that there
445 was sufficient time for differentiation to EPI and PrE, we thawed blastocysts at 5dpf or

446 6dpf and cultured them for 16 hours. All information on embryo score and
447 developmental day and stage at time of cryopreservation can be found in
448 Supplementary Table 28. The latter marker was chosen to demonstrate that the
449 transcriptomic signature of p53 signalling is caused by DNA-damage-induced
450 phosphorylation of Serine-15 on p53 (Loughery *et al.*, 2014). Aneuploid embryos
451 showed a higher percentage of cells with activated p53 (Fig. 4b,c), as suggested by
452 our transcriptomic data (Figure 1), although these differences did not reach
453 significance when considering the ICM/EPI (OCT4-positive) cells or TE (OCT4-
454 negative) separately (Supplementary Fig. 2a-c). We then investigated cell type
455 specificity of proliferative defects and apoptosis. Both the aneuploid TE and OCT4-
456 positive cells showed decreased cell numbers (Fig. 4d-f) that led to an overall decrease
457 of cell numbers in whole aneuploid embryos (Fig. 4g), confirming our previous
458 experiment (Fig. 3g). The observed increased percentage of nuclear CASP3/7 positive
459 cells in the TE of aneuploid embryos (Fig. 4h,i) and increased CASP3/7 mean intensity
460 per cell in whole aneuploid embryos (Fig. 4h,j) points to apoptosis as the cause of this
461 decrease in cell numbers. However, no OCT4-positive cells of either euploid or
462 aneuploid group showed nuclear CASP3/7 signal (Fig. 4h). We also found CASP3/7-
463 positive micronuclei which were increased in number in aneuploid embryos (Fig. 4h,
464 Supplementary Fig. 2d,e).

465 The observation (figure 4f) that the ICM/EPI cell numbers of aneuploid embryos fell
466 into two groups with either low or high cell counts led us to further investigate the
467 impact of aneuploidies on the second lineage segregation event. All blastocysts were
468 re-stained for GATA4 (PrE marker) and imaged together with OCT4 (ICM/EPI marker).
469 We found that while all euploid embryos contained GATA4-positive cells, 7/14
470 aneuploid embryos had no GATA4-positive cells (Fig. 4k,l) and that in those with

471 GATA4-positive PrE cells, there was a significantly lower ratio of GATA4-positive to
472 OCT4-positive/GATA4-negative cells (Fig. 4m). In line with their decreased ICM cell
473 numbers and absence of PrE, the aneuploid embryos had received a significantly lower
474 ICM score by the clinical embryologists at time of cryopreservation (1xA/13xB) when
475 compared to euploid embryos (6xA/4xB, p=0.0088, Fisher-exact test).

476 We then investigated whether there are different levels of LC3B as marker of
477 autophagy between the aneuploid TE and ICM in an additional 5 aneuploid and 4
478 euploid embryos. Aneuploid embryos displayed increased levels of autophagy mainly
479 attributable to the TE (Fig. 4n-q), while their ICM/EPI cells showed a small increase in
480 autophagy which did not reach significance (Fig. 4q). The aneuploid embryos could be
481 separated in two groups: a first group with low levels of autophagy lacking GATA4-
482 positive cells in 2 out of 3 embryos (Fig. 4n, left and right panels, 2nd row) and a high-
483 level autophagy group in which both embryos contained GATA4-positive cells (Fig. 4n,
484 left and right panels 3rd row).

485 Lastly, we separated the aneuploid embryos into a low- and a high-dosage group as
486 done for the gene-expression analysis (Supplementary Table 29). Trend analysis
487 showed that the higher the number of imbalanced loci, the lower the cell numbers in
488 the TE and PrE but not in the EPI (Fig. 4r).

489 **Discussion**

490 In this work, we studied the consequences of aneuploidy in human preimplantation
491 embryos that carried a uniformly present, presumed meiotic, complex aneuploidy. In
492 our study we find that, while aneuploid embryos had lower cell numbers in both TE and
493 ICM/EPI, the effect of aneuploidy was cell-type dependent. Aneuploid TE presented
494 transcriptomic signatures of p53 signalling and apoptosis, and immunostaining of
495 whole embryos showed that aneuploidy results in increased proteotoxic stress,
496 autophagy, DNA damage-mediated activated p53 and subsequent apoptosis in the TE.
497 In contrast, aneuploidy impairs the second lineage differentiation and affects PrE
498 formation in particular.

499 Overall, our gene-expression results are in line with previously published RNA-
500 sequencing studies on aneuploid human embryonic cells that identified transcriptional
501 signatures consistent with DNA damage (Vera-Rodriguez *et al.*, 2015; Licciardi *et al.*,
502 2018; Fuchs Weizman *et al.*, 2019), alteration of cell proliferation (Starostik *et al.*, 2020;
503 Maxwell *et al.*, 2022; Martin *et al.*, 2023), the cell cycle (Vera-Rodriguez *et al.*, 2015;
504 Licciardi *et al.*, 2018; Fuchs Weizman *et al.*, 2019; Starostik *et al.*, 2020; Martin *et al.*,
505 2023), deregulation of autophagy (Licciardi *et al.*, 2018; Sanchez-Ribas *et al.*, 2019),
506 p53 signalling (Licciardi *et al.*, 2018) and apoptosis (Licciardi *et al.*, 2018; Groff *et al.*,
507 2019; Sanchez-Ribas *et al.*, 2019; Maxwell *et al.*, 2022; Martin *et al.*, 2023). However,
508 when comparing our dataset of differentially expressed genes to these studies, we only
509 found modest overlaps at the level of individual genes. This is probably because
510 embryos of different developmental stages were included in the studies, containing
511 specific aneuploidies, and of different sample types (overview in Supplementary Table
512 17). Naturally acquired and induced aneuploidies only share a few differentially
513 expressed genes but show overall equal signatures after pathway analysis, suggesting

514 that reversine-based models of aneuploidy are very close but may not fully mimic
515 endogenous aneuploidy. We also observed aneuploidy-mediated gene dosage effects
516 in the TE cells, as extensively reported in human and mouse aneuploid cancer cell
517 lines (Dürrbaum and Storchová, 2016), and found that a higher dosage leads to
518 stronger p53 signalling and apoptosis responses.

519 We next tested the predictions made based on the gene-expression profiles with
520 immunostaining. First, we found evidence of proteotoxic stress and increased
521 expression of autophagy proteins, as well as activation of apoptosis. The most likely
522 series of events is that p62/LC3B/CASP8 interaction results in autophagy-mediated
523 apoptosis in aneuploid human embryos. Nevertheless, we cannot rule out indirect
524 activation of apoptosis mediated by autophagy due to the degradation of cell
525 organelles (Gump and Thorburn, 2011). This is supported by the observation in the
526 aneuploid mouse embryo model that autophagy is independent of the mTOR pathway
527 (Singla *et al*., 2020). Other upstream regulators of autophagy could be involved, such
528 as the cGAS-STING pathway (Krivega *et al.*, 2021) or, as also observed in our dataset,
529 p53-mediated activation of DRAM1 (Crighton *et al.*, 2006) that can induce apoptosis
530 by increasing BAX protein levels (Guan *et al.*, 2015). Second, we confirmed the
531 presence of activated *p53* in aneuploid human embryos. We specifically stained for
532 p53 with phosphorylation on Serine 15, mediated by kinases such as ATM and ATR
533 as a direct result of DNA-damage (Loughery *et al*., 2014). This indicates that
534 aneuploidy also induces the DNA-damage response in the embryo, as found in the
535 mouse and 2D gastruloids (Singla *et al.*, 2020; Yang *et al.*, 2021). An interesting
536 observation is that aneuploid embryos contained increased numbers of CASP3/7
537 positive micronuclei. This is similar to findings in a non-human primate model showing
538 that abnormal chromosomes can be encapsulated in micronuclei, which can

539 subsequently be selectively eliminated from the embryo (Daughtry *et al.*, 2019). In
540 human cleavage stage embryos these micronuclei have been shown to contain genetic
541 material that originates from chromosome breakages due to replication fork stalling
542 and DNA-damage (Palmerola *et al.*, 2022), further highlighting how aneuploidy is
543 leading to DNA-damage in the human embryo. In sum, our results in this part are in
544 line with previous findings on mouse and 2D gastruloid models (Singla *et al.*, 2020;
545 Yang *et al.*, 2021), and suggest that these conserved stress responses to aneuploidy
546 are also activated in fully aneuploid embryos with complex karyotypes, both converging
547 on apoptosis if not resolved. First, proteotoxic stress resulting from gene-dosage
548 imbalances mediates the unfolded protein response and autophagy, and second,
549 replication stress that can lead to DNA-damage, resulting in p53 activation and
550 ultimately to apoptosis (Li *et al.*, 2010; Thompson and Compton, 2010; Santaguida *et*
551 *al.*, 2015, 2017; Zhu *et al.*, 2018; Chunduri and Storchová, 2019; Krivega *et al.*, 2022;
552 Regin *et al.*, 2022).

553 In the second part of our work, we focused on studying the lineage-specific response
554 to complex aneuploidy, as the studies on reversine-treated mouse embryos (Bolton *et*
555 *al.*, 2016; Singla *et al.*, 2020) and human 2D gastruloids (Yang *et al.*, 2021) also
556 identified a cell-type specific effect of aneuploidy. In the mouse, aneuploid cells are
557 eliminated by apoptosis in the EPI, while tolerated in the TE, and in human 2D
558 gastruloids, aneuploid cells are eliminated in the post-gastrulation embryonic germ
559 layers but tolerated in the TE. We found lower cell numbers and increased apoptosis
560 in aneuploid TE cells. While we also detected lower cell numbers in aneuploid OCT4-
561 positive ICM/EPI, we did not find any of them to be CASP3/7 positive, i.e. undergoing
562 apoptosis. These results are in line with the findings of Victor *et al*. (Victor *et al.*, 2019),
563 where the TE of mosaic and aneuploid embryos showed increased levels of apoptosis,

564 and the recent RNA-sequencing of TE and ICM samples of mosaic human embryos
565 (Martin *et al.*, 2023). Mosaic TE cells showed disrupted regulation of apoptosis while
566 the ICM showed primarily deregulated mitochondrial function. However, in contrast to
567 our findings, some of the embryos in the study of Victor et al. showed CASP3/7 positive
568 signals in the ICM; further research will be needed to understand if these differences
569 with our findings and those of Martin *et al.* are related to technical or to biological
570 factors. Finally, the differences with the mouse results are possibly due to species-
571 specific properties of the ICM/EPI cells. For instance, the lack of apoptosis in the
572 human ICM/EPI could be due to an uncoupling between aneuploidy-induced stress
573 signals and apoptosis, as observed in human embryonic stem cells (Mantel *et al.*,
574 2007). In this context, the lower cell numbers in aneuploid embryos could be explained
575 by two other known effects of *p53* activation which are not apoptosis. First, *p53*
576 activation could decrease cell proliferation, leading to lower cell numbers. Secondly,
577 *p53* activation may downregulate *OCT4* and *NANOG* expression, as seen in mouse
578 embryonic stem cells (Lin *et al.*, 2005), leading to loss of pluripotency and driving the
579 cells to differentiation and out of the ICM/EPI.

580 Another difference is that we found that the human aneuploid TE had increased levels
581 of autophagy markers, which did not reach statistical significance in the ICM/EPI, while
582 the mouse EPI does show increased autophagy (Singla *et al.*, 2020). Interestingly, the
583 aneuploid OCT4-positive cells separated into a high and a low-level autophagy group,
584 where the low-level group seemed to lack GATA4-positive PrE cells. Although based
585 on a few samples, this data suggests that an ICM in a transcriptionally earlier state of
586 pluripotency, i.e. GATA4-negative and prior to the second lineage segregation event,
587 might be less sensitive to the consequences of aneuploidy, i.e. show less autophagy.
588 We thus propose that aneuploid human embryonic cells in the ICM become more

589 sensitive from the second lineage segregation onwards. We hypothesize that this
590 effect may even become stronger and more specific to the embryonic lineage after
591 onset of gastrulation, as elegantly shown in human 2D gastruloids (Yang *et al.*, 2021).

592 Finally, we found that in those embryos that had already undergone the second lineage
593 segregation event, the aneuploid embryos had a significantly lower ratio of PrE
594 (GATA4-positive) to EPI (OCT4-positive/GATA4-negative) cells than euploid embryos.
595 Our findings are in line with the upregulation of the PrE marker *SOX17* that has been
596 recently found by gene-expression analysis of euploid and low- and high level mosaic
597 human embryos (Martin *et al.*, 2023). Further, we observed that this effect was dosage-
598 dependent, with embryos with larger gene-dosage imbalances showing significantly
599 lower cell numbers in the TE and PrE than euploid embryos or embryos with lower
600 gene-dosage imbalances. This suggests that complex aneuploidy both affects TE and
601 ICM proliferation and PrE formation or that the PrE is more sensitive to aneuploidy-
602 mediated apoptosis than the less differentiated EPI. An alternative explanation is that
603 in aneuploid human embryos the PrE forms at a later time point due to their delayed
604 development. In our study, to minimize the risk of missing the second lineage
605 segregation, we purposefully used 5-6dpf expanded blastocysts that were kept in
606 culture for an additional 16 hours after warming, to allow the embryos sufficient time to
607 recover and develop.

608 When interpreting the results of this study, it is important to bear in mind that we
609 identified the ICM/EPI as staining positive for OCT4 and the PrE as positive for GATA4.
610 We confirmed that the embryos analysed were expanded blastocysts which had
611 undergone the first lineage segregations, as OCT4 was restricted to the inner cells and
612 absent in TE cells (Niakan and Eggan, 2013). The identity of human ICM and EPI cells
613 is currently under vigorous debate (Meistermann *et al.*, 2021; Radley *et al.*, 2022) and

614 exclusive markers of either cell type are untested. Therefore we cannot assign ICM or
615 EPI identity to OCT4-positive cells. However, in blastocysts with GATA4-positive cells
616 the second lineage segregation had occurred and PrE was established, and
617 consequently we confidently assigned the EPI identity to OCT4-positive cells in these
618 blastocysts. In GATA4-negative embryos OCT4-positive cells could be either ICM or
619 EPI cells. Interestingly, we never found GATA4-positive cells in the absence of OCT4-
620 positive cells, supporting the hypothesis that PrE cells differentiate from EPI cells
621 (Meistermann *et al.*, 2021). Limitations of our study are that we did not analyse the
622 transcriptome of the ICM of our embryos, because after the biopsy they were used for
623 immunostainings instead, and we can therefore not draw any conclusions on their
624 transcriptome. We did not study embryos with the same type of aneuploidy and can
625 thus not provide insight on chromosome-specific effects. Although some of our
626 embryos carried genetic abnormalities in mosaic form as part of their complex
627 karyotype (aneuploid/aneuploid mosaics), we did not study diploid/aneuploid mosaic
628 embryos and can therefore not assert that these also activate the same cellular stress
629 pathways in their aneuploid cells. Since these pathways are common to most cell
630 types, our guess would however be that they are activated in mosaic embryos too.
631 Lastly, the possibilities for functional studies and lineage tracing experiments in human
632 embryos are very limited, which is why we can only present an observational study.

633 Taken together, our results suggest that while the same pathways appear to be
634 activated in human and mouse embryos with complex aneuploidy, human embryos
635 have a different response when it comes to the downstream effect of these pathways
636 in the different cell lineages. While the mouse readily depletes aneuploid cells by
637 apoptosis specifically from the embryonic lineage before implantation (Bolton *et al.*,
638 2016; Singla *et al.*, 2020), in the preimplantation human embryo, apoptosis appears to

639 be more active in the TE, as also seen by others (Victor *et al.*, 2019; Martin *et al.*,
640 2023). The results suggest that in the human embryo, undifferentiated pluripotent cells
641 have a different response to aneuploidy-induced cellular stress than the neighbouring
642 differentiated cells.

643 Our results on human embryos with complex meiotic aneuploidy provide further insight
644 into the mechanisms by which human embryos respond to gene-dosage imbalances,
645 and may contribute to understanding how aneuploid cells are selectively eliminated in
646 mosaic embryos. Further research, especially by using human embryos with
647 endogenous chromosomal mosaicism, will be needed to shed light on the interactions
648 between proteotoxic stress, the p53 pathway and differentiation during early
649 development, for which the most novel models of human embryo implantation
650 (Deglincerti *et al.*, 2016; Shahbazi *et al.*, 2016, 2020; Kagawa *et al.*, 2021) will prove
651 to be of incalculable value.

652

References

Ariyoshi K, Miura T, Kasai K, Fujishima Y, Oshimura M, Yoshida MA. Induction of genomic instability and activation of autophagy in artificial human aneuploid cells. *Mutat Res* [Internet] 2016;**790**:19–30. Mutat Res.

Banin S, Moyal L, Shieh SY, Taya Y, Anderson CW, Chessa L, Smorodinsky NI, Prives C, Reiss Y, Shiloh Y, *et al.* Enhanced phosphorylation of p53 by ATM in response to DNA damage. *Science* [Internet] 1998;**281**:1674–1677. Science.

Bolton H, Graham SJL, Aa N Van Der, Kumar P, Theunis K, Fernandez Gallardo E, Voet T, Zernicka-Goetz M. Mouse model of chromosome mosaicism reveals lineage-specific depletion of aneuploid cells and normal developmental potential. *Nat Commun* [Internet] 2016;**7**:1–12. Nature Publishing Group.

Capalbo A, Poli M, Rienzi L, Girardi L, Patassini C, Fabiani M, Cimadomo D, Benini F, Farcomeni A, Cuzzi J, *et al.* Mosaic human preimplantation embryos and their developmental potential in a prospective , non-selection clinical trial. 2021;1–10.

Capalbo A, Wright G, Elliott T, Ubaldi FM, Rienzi L, Nagy ZP. FISH reanalysis of inner cell mass and trophectoderm samples of previously array-CGH screened blastocysts shows high accuracy of diagnosis and no major diagnostic impact of mosaicism at the blastocyst stage. *Human Reproduction* 2013;**28**:2298–2307. Oxford University Press.

Chavez SL, Loewke KE, Han J, Moussavi F, Colls P, Munne S, Behr B, Reijo Pera RA. Dynamic blastomere behaviour reflects human embryo ploidy by the four-cell stage. *Nat Commun* [Internet] 2012;**3**:. Nat Commun.

Chow JFC, Yeung WSB, Lau EYL, Lee VCY, Ng EHY, Ho PC. Array comparative genomic hybridization analyses of all blastomeres of a cohort of embryos from young IVF patients revealed significant contribution of mitotic errors to embryo mosaicism at the cleavage stage. *Reprod Biol Endocrinol* [Internet] 2014;**12**:. Reprod Biol Endocrinol.

Chunduri NK, Barthel K, Storchova Z. Consequences of Chromosome Loss: Why Do Cells Need Each Chromosome Twice? *Cells 2022, Vol 11, Page 1530* [Internet] 2022;**11**:1530. Multidisciplinary Digital Publishing Institute.

Chunduri NK, Storchová Z. The diverse consequences of aneuploidy. *Nat Cell Biol* [Internet] 2019;**21**:54–62. Nature Publishing Group.

Coorens THH, Oliver TRW, Sanghvi R, Sovio U, Cook E, Vento-Tormo R, Haniffa M, Young MD, Rahbari R, Sebire N, *et al.* Inherent mosaicism and extensive mutation of human placentas. *Nature* 2021;**592**:80–85. Nature Research.

Crighton D, Wilkinson S, O'Prey J, Syed N, Smith P, Harrison PR, Gasco M, Garrone O, Crook T, Ryan KM. DRAM, a p53-Induced Modulator of Autophagy, Is Critical for Apoptosis. *Cell* 2006;**126**:121–134. Elsevier B.V.

701 Daughtry BL, Rosenkrantz JL, Lazar NH, Fei SS, Redmayne N, Torkenczy KA, Adey
702 A, Yan M, Gao L, Park B, *et al.* Single-cell sequencing of primate
703 preimplantation embryos reveals chromosome elimination via cellular
704 fragmentation and blastomere exclusion. *Genome Res* [Internet] 2019;**29**:367–
705 382. Cold Spring Harbor Laboratory Press.
706
707 David K Gardner, William B Schoolcraft. Culture and transfer of human blastocysts.
708 *Curr Opin Obstet Gynecol* 1999;**11**:307–311.
709
710 Deglincerti A, Croft GF, Pietila LN, Zernicka-Goetz M, Siggia ED, Brivanlou AH. Self-
711 organization of the in vitro attached human embryo. *Nature* [Internet]
712 2016;**533**:251–254.
713
714 Dobin A, Davis CA, Schlesinger F, Drenkow J, Zaleski C, Jha S, Batut P, Chaisson
715 M, Gingeras TR. STAR: ultrafast universal RNA-seq aligner. *Bioinformatics*
716 2013;**29**:15–21.
717
718 Donnelly N, Passerini V, Dürrbaum M, Stingele S, Storchová Z. HSF1 deficiency and
719 impaired HSP90-dependent protein folding are hallmarks of aneuploid human
720 cells. *EMBO J* [Internet] 2014;**33**:2374. European Molecular Biology
721 Organization.
722
723 Dürrbaum M, Kuznetsova A, Passerini V, Stingele S, Stoehr G, Storchová Z. Unique
724 features of the transcriptional response to model aneuploidy in human cells.
725 *BMC Genomics* [Internet] 2014;**15**:139. BioMed Central.
726
727 Dürrbaum M, Storchová Z. Effects of aneuploidy on gene expression: implications for
728 cancer. *FEBS J* [Internet] 2016;**283**:791–802. John Wiley & Sons, Ltd.
729
730 Echten-Arends J van, Mastenbroek S, Sikkema-Raddatz B, Korevaar JC, Heineman
731 MJ, Veen F van der, Repping S. Chromosomal mosaicism in human
732 preimplantation embryos: a systematic review. *Hum Reprod Update* [Internet]
733 2011;**17**:620–627. Oxford University Press.
734
735 Fragouli E, Alfarawati S, Spath K, Babariya D, Tarozzi N, Borini A, Wells D. Analysis
736 of implantation and ongoing pregnancy rates following the transfer of mosaic
737 diploid–aneuploid blastocysts. *Hum Genet* [Internet] 2017;**136**:805–819.
738 Springer Verlag.
739
740 Fragouli E, Munne S, Wells D. The cytogenetic constitution of human blastocysts:
741 insights from comprehensive chromosome screening strategies. *Hum Reprod*
742 *Update* [Internet] 2019;**25**:15–33. Oxford University Press.
743
744 Fuchs Weizman N, Wyse BA, Antes R, Ibarrientos Z, Sangaralingam M, Motamedi
745 G, Kuznyetsov V, Madjunkova S, Librach CL. Towards Improving Embryo
746 Prioritization: Parallel Next Generation Sequencing of DNA and RNA from a
747 Single Trophectoderm Biopsy. *Sci Rep* [Internet] 2019;**9**:1–11. Nature Publishing
748 Group.
749

Greco E, Minasi MG, Fiorentino F. Healthy Babies after Intrauterine Transfer of Mosaic Aneuploid Blastocysts. *New England Journal of Medicine* [Internet] 2015;**373**:2089–2090. Massachusetts Medical Society.

Griffin DK, Brezina PR, Tobler K, Zhao Y, Silvestri G, Mccoy RC, Anchan R, Benner A, Cutting GR, Kearns WG. The human embryonic genome is karyotypically complex, with chromosomally abnormal cells preferentially located away from the developing fetus. *Human Reproduction* [Internet] 2022; Oxford University Press (OUP)

Groff AF, Resetkova N, DiDomenico F, Sakkas D, Penzias A, Rinn JL, Eggan K. RNA-seq as a tool for evaluating human embryo competence. *Genome Res* [Internet] 2019;**29**:1705–1718. Cold Spring Harbor Laboratory Press.

Guan JJ, Zhang XD, Sun W, Qi L, Wu JC, Qin ZH. DRAM1 regulates apoptosis through increasing protein levels and lysosomal localization of BAX. *Cell Death Dis* [Internet] 2015;**6**:e1624–e1624. Nature Publishing Group.

Gump JM, Thorburn A. Autophagy and apoptosis: what is the connection? *Trends Cell Biol* [Internet] 2011;**21**:387–392. Trends Cell Biol.

Huettel B, Kreil DP, Matzke M, Matzke AJM. Effects of aneuploidy on genome structure, expression, and interphase organization in Arabidopsis thaliana. *PLoS Genet* [Internet] 2008;**4**:. PLoS Genet.

Jacobs K, Velde H van de, Paepe C de, Sermon K, Spits C. Mitotic spindle disruption in human preimplantation embryos activates the spindle assembly checkpoint but not apoptosis until Day 5 of development. *MHR: Basic science of reproductive medicine* [Internet] 2017;**23**:321–329. Oxford University Press.

Jaiswal SK, Raj S, DePamphilis ML. Developmental Acquisition of p53 Functions. *Genes (Basel)* [Internet] 2021;**12**:1675. MDPI.

Johnson DS, Cinnioglu C, Ross R, Filby A, Gemelos G, Hill M, Ryan A, Smotrich D, Rabinowitz M, Murray MJ. Comprehensive analysis of karyotypic mosaicism between trophectoderm and inner cell mass. *MHR: Basic science of reproductive medicine* [Internet] 2010;**16**:944–949. Oxford University Press.

Kagawa H, Javali A, Khoei HH, Sommer TM, Sestini G, Novatchkova M, Scholte op Reimer Y, Castel G, Bruneau A, Maenhoudt N, *et al.* Human blastoids model blastocyst development and implantation. *Nature* [Internet] 2021;1–9. Nature Publishing GroupAvailable fr

Kalousek DK, Vekemans M. Confined placental mosaicism. *J Med Genet* [Internet] 1996;**33**:529–533. BMJ Publishing Group.

Krivega M, Stiefel CM, Karbassi S, Andersen LL, Chunduri NK, Donnelly N, Pichlmair A, Storchová Z. Genotoxic stress in constitutive trisomies induces autophagy and the innate immune response via the cGAS-STING pathway. *Communications Biology 2021 4:1* [Internet] 2021;**4**:1–16. Nature Publishing Group.

Krivega M, Stiefel CM, Storchova Z. Consequences of chromosome gain: A new view on trisomy syndromes. *Am J Hum Genet* 2022;**109**:2126–2140. Cell Press.

Landuyt L Van, Stoop D, Verheyen G, Verpoest W, Camus M, Velde H Van De, Devroey P, Abbeel E Van Den. Outcome of closed blastocyst vitrification in relation to blastocyst quality: Evaluation of 759 warming cycles in a single-embryo transfer policy. *Human Reproduction* 2011;**26**:527–534. Oxford University Press.

Li B, Dewey CN. RSEM: accurate transcript quantification from RNA-Seq data with or without a reference genome. *BMC Bioinformatics* 2011;**12**:323.

Li M, Fang X, Baker DJ, Guo L, Gao X, Wei Z, Han S, Deursen JM Van, Zhang P. The ATM-p53 pathway suppresses aneuploidy-induced tumorigenesis. *Proc Natl Acad Sci U S A* [Internet] 2010;**107**:14188–14193. National Academy of Sciences.

Licciardi F, Lhakhang T, Kramer YG, Zhang Y, Heguy A, Tsirigos A. Human blastocysts of normal and abnormal karyotypes display distinct transcriptome profiles. *Sci Rep* [Internet] 2018;**8**:1–9. Nature Publishing Group.

Lin T, Chao C, Saito S, Mazur SJ, Murphy ME, Appella E, Xu Y. p53 induces differentiation of mouse embryonic stem cells by suppressing Nanog expression. *Nat Cell Biol* [Internet] 2005;**7**:165–171. Nat Cell Biol.

Loughery J, Cox M, Smith LM, Meek DW. Critical role for p53-serine 15 phosphorylation in stimulating transactivation at p53-responsive promoters. *Nucleic Acids Res* [Internet] 2014;**42**:7666–7680. Oxford University Press.

Love MI, Huber W, Anders S. Moderated estimation of fold change and dispersion for RNA-seq data with DESeq2. *Genome Biol* 2014;**15**:. BioMed Central Ltd.

Mantel C, Guo Y, Lee MR, Kim M-K, Han M-K, Shibayama H, Fukuda S, Yoder MC, Pelus LM, Kim K-S, *et al.* Checkpoint-apoptosis uncoupling in human and mouse embryonic stem cells: a source of karyotpic instability. *Blood* [Internet] 2007;**109**:4518–4527.

Martin A, Mercader A, Dominguez F, Quiñonero A, Perez M, Gonzalez-Martin R, Delgado A, Mifsud A, Pellicer A, Los Santos MJ De. Mosaic results after preimplantation genetic testing for aneuploidy may be accompanied by changes in global gene expression. *Front Mol Biosci* [Internet] 2023;**10**:264. Frontiers.

850 Maxwell SM, Lhakhang TC, Lin Z, Kramer YG, Zhang Y, Wang F, Heguy A, Tsirigos
851 A, Grifo JA, Licciardi F. Investigation of Global Gene Expression of Human
852 Blastocysts Diagnosed as Mosaic using Next-generation Sequencing.
853 *Reproductive Sciences* [Internet] 2022;1–11. Springer
854
855 McCoy RC. Mosaicism in Preimplantation Human Embryos: When Chromosomal
856 Abnormalities Are the Norm. *Trends in Genetics* [Internet] 2017;**33**:448–463.
857 Elsevier.
858
859 Meistermann D, Bruneau A, Loubersac S, Reignier A, Firmin J, François-Campion V,
860 Kilens S, Lelièvre Y, Lammers J, Feyeux M, *et al.* Integrated pseudotime
861 analysis of human pre-implantation embryo single-cell transcriptomes reveals
862 the dynamics of lineage specification. *Cell Stem Cell* 2021;**28**:1625-1640.e6.
863
864 Mertzanidou A, Spits C, Nguyen HT, Velde H van de, Sermon K. Evolution of
865 aneuploidy up to Day 4 of human preimplantation development. *Human*
866 *Reproduction* [Internet] 2013a;**28**:1716–1724. Oxford University Press.
867
868 Mertzanidou A, Wilton L, Cheng J, Spits C, Vanneste E, Moreau Y, Vermeesch JR,
869 Sermon K. Microarray analysis reveals abnormal chromosomal complements in
870 over 70% of 14 normally developing human embryos. *Human Reproduction*
871 [Internet] 2013b;**28**:256–264. Oxford University Press.
872
873 Munné S, Blazek J, Large M, Martinez-Ortiz PA, Nisson H, Liu E, Tarozzi N, Borini A,
874 Becker A, Zhang J, *et al.* Detailed investigation into the cytogenetic constitution
875 and pregnancy outcome of replacing mosaic blastocysts detected with the use of
876 high-resolution next-generation sequencing. *Fertil Steril* [Internet] 2017;**108**:62-
877 71.e8. Elsevier Inc.
878
879 Munné S, Nakajima ST, Najmabadi S, Sauer M v., Angle MJ, Rivas JL, Mendieta L
880 v., MacAso TM, Sawarkar S, Nadal A, *et al.* First PGT-A using human in vivo
881 blastocysts recovered by uterine lavage: Comparison with matched IVF embryo
882 controls. *Human Reproduction* [Internet] 2020a;**35**:70–80. Oxford University
883 Press.
884
885 Munné S, Spinella F, Grifo J, Zhang J, Beltran MP, Fragouli E, Fiorentino F. Clinical
886 outcomes after the transfer of blastocysts characterized as mosaic by high
887 resolution Next Generation Sequencing- further insights. *Eur J Med Genet*
888 2020b;**63**:103741. Elsevier Masson SAS.
889
890 Niakan KK, Eggan K. Analysis of human embryos from zygote to blastocyst reveals
891 distinct gene expression patterns relative to the mouse. *Dev Biol* [Internet]
892 2013;**375**:54–64. Dev Biol.
893
894 Ohashi A, Ohori M, Iwai K, Nakayama Y, Nambu T, Morishita D, Kawamoto T,
895 Miyamoto M, Hirayama T, Okaniwa M, *et al.* Aneuploidy generates proteotoxic
896 stress and DNA damage concurrently with p53-mediated post-mitotic apoptosis
897 in SAC-impaired cells. *Nat Commun* [Internet] 2015;**6**:1–16. Nature Publishing
898 Group.
899

900 Oromendia AB, Dodgson SE, Amon A. Aneuploidy causes proteotoxic stress in
901 yeast. *Genes Dev* 2012;**26**:2696–2708.
902
903 Orvieto R, Shimon C, Rienstein S, Jonish-Grossman A, Shani H, Aizer A. Do human
904 embryos have the ability of self-correction? *Reprod Biol Endocrinol* [Internet]
905 2020;**18**:. Reprod Biol Endocrinol.
906
907 Palmerola KL, Amrane S, Los Angeles A de, Xu S, Wang N, Pinho J de, Zuccaro M
908 v, Taglialatela A, Massey DJ, Turocy J, *et al.* Replication stress impairs
909 chromosome segregation and preimplantation development in human embryos.
910 *Cell* [Internet] 2022;
911
912 Pan J-A, Ullman E, Dou Z, Zong W-X. Inhibition of protein degradation induces
913 apoptosis through a microtubule-associated protein 1 light chain 3-mediated
914 activation of caspase-8 at intracellular membranes. *Mol Cell Biol* [Internet]
915 2011;**31**:3158–3170. American Society for Microbiology.
916
917 Popovic M, Dhaenens L, Boel A, Menten B, Heindryckx B. Chromosomal mosaicism
918 in human blastocysts: The ultimate diagnostic dilemma. *Hum Reprod Update*
919 [Internet] 2020;**26**:313–334. Oxford University Press.
920
921 Popovic M, Dheedene A, Christodoulou C, Taelman J, Dhaenens L, Nieuwerburgh F
922 Van, Deforce D, Abbeel E Van Den, Sutter P De, Menten B, *et al.* Chromosomal
923 mosaicism in human blastocysts: The ultimate challenge of preimplantation
924 genetic testing? *Human Reproduction* [Internet] 2018;**33**:1342–1354. Oxford
925 University Press.
926
927 Radley A, Corujo-Simon E, Nichols J, Smith A, Dunn SJ. Entropy sorting of single-
928 cell RNA sequencing data reveals the inner cell mass in the human pre-
929 implantation embryo. *Stem Cell Reports* [Internet] 2022;**0**: Cell Press.
930
931 Regin M, Spits C, Sermon K. On the origins and fate of chromosomal abnormalities
932 in human preimplantation embryos: an unsolved riddle. *Mol Hum Reprod*
933 [Internet] 2022; Mol Hum Reprod
934
935 Ren Y, Yan Z, Yang M, Keller L, Zhu X, Lian Y, Liu Q, Li R, Zhai F, Nie Y, *et al.*
936 Regional and developmental characteristics of human embryo mosaicism
937 revealed by single cell sequencing. *PLoS Genet* 2022;**18**:. Public Library of
938 Science.
939
940 Ritchie ME, Phipson B, Wu D, Hu Y, Law CW, Shi W, Smyth GK. Limma powers
941 differential expression analyses for RNA-sequencing and microarray studies.
942 *Nucleic Acids Res* [Internet] 2015;**43**:e47. Oxford University Press.
943
944 Robinson MD, McCarthy DJ, Smyth GK. edgeR: A Bioconductor package for
945 differential expression analysis of digital gene expression data. *Bioinformatics*
946 2009;**26**:139–140. Oxford University Press.
947
948
949 Robinson MD, Oshlack A. *A scaling normalization method for differential expression*
950 *analysis of RNA-seq data* [Internet]. 2010

951 Sanchez-Ribas I, Diaz-Gimeno P, Sebastián-León P, Mercader A, Quiñonero A,
952 Ballesteros A, Pellicer A, Domínguez F. Transcriptomic behavior of genes
953 associated with chromosome 21 aneuploidies in early embryo development.
954 *Fertil Steril* 2019;**111**:991-1001.e2. Elsevier Inc.
955
956 Santaguida S, Amon A. Short- and long-term effects of chromosome mis-segregation
957 and aneuploidy. *Nat Rev Mol Cell Biol* [Internet] 2015;**16**:473–485. Nature
958 Publishing Group.
959
960 Santaguida S, Richardson A, Iyer DR, M'Saad O, Zasadil L, Knouse KA, Wong YL,
961 Rhind N, Desai A, Amon A. Chromosome Mis-segregation Generates Cell-
962 Cycle-Arrested Cells with Complex Karyotypes that Are Eliminated by the
963 Immune System. *Dev Cell* 2017;**41**:638-651.e5. Cell Press.
964
965 Santaguida S, Vasile E, White E, Amon A. Aneuploidy-induced cellular stresses limit
966 autophagic degradation. *Genes Dev* [Internet] 2015;**29**:2010–2021. Cold Spring
967 Harbor Laboratory Press.
968
969 Shahbazi MN, Jedrusik A, Vuoristo S, Recher G, Hupalowska A, Bolton V, Fogarty
970 NME, Campbell A, Devito LG, Ilic D, *et al.* Self-organization of the human
971 embryo in the absence of maternal tissues. *Nat Cell Biol* [Internet] 2016;**18**:700–
972 708. Nature Publishing Group.
973
974 Shahbazi MN, Wang T, Tao X, Weatherbee BAT, Sun L, Zhan Y, Keller L, Smith GD,
975 Pellicer A, Scott RT, *et al.* Developmental potential of aneuploid human embryos
976 cultured beyond implantation. *Nat Commun* [Internet] 2020;**11**:1–15. Nature
977 Research.
978
979 Singla S, Iwamoto-Stohl LK, Zhu M, Zernicka-Goetz M. Autophagy-mediated
980 apoptosis eliminates aneuploid cells in a mouse model of chromosome
981 mosaicism. *Nat Commun* [Internet] 2020;**11**:1–15. Nature Research.
982
983 Starostik MR, Sosin OA, McCoy RC. Single-cell analysis of human embryos reveals
984 diverse patterns of aneuploidy and mosaicism. *Genome Res* 2020;**30**:814–826.
985
986 Stingele S, Stoehr G, Peplowska K, Cox J, Mann M, Storchova Z. Global analysis of
987 genome, transcriptome and proteome reveals the response to aneuploidy in
988 human cells. *Mol Syst Biol* [Internet] 2012;**8**:608. EMBO Press.
989
990 Tang YC, Williams BR, Siegel JJ, Amon A. Identification of Aneuploidy-Selective
991 Antiproliferation Compounds. *Cell* 2011;**144**:499–512. Cell Press.
992
993 Thompson SL, Compton DA. Proliferation of aneuploid human cells is limited by a
994 p53-dependent mechanism. *J Cell Biol* [Internet] 2010;**188**:369–381. J Cell Biol.
995
996 Torres EM, Sokolsky T, Tucker CM, Chan LY, Boselli M, Dunham MJ, Amon A.
997 Effects of aneuploidy on cellular physiology and cell division in haploid yeast.
998 *Science (1979)* [Internet] 2007;**317**:916–924. American Association for the
999 Advancement of Science
1000

1001 Vanneste E, Voet T, Caignec C le, Ampe M, Konings P, Melotte C, Debrock S,
1002 Amyere M, Vikkula M, Schuit F, *et al.* Chromosome instability is common in
1003 human cleavage-stage embryos. *Nat Med* [Internet] 2009;**15**:577–583. Nature
1004 Publishing Group.
1005
1006 van Echten-Arends J, Mastenbroek S, Sikkema-Raddatz B, Korevaar JC, Heineman
1007 MJ, van der Veen F, Repping S. Chromosomal mosaicism in human
1008 preimplantation embryos: a systematic review. Hum Reprod Update. 2011 Sep-
1009 Oct;17(5):620-7. doi: 10.1093/humupd/dmr014. Epub 2011 Apr 29. PMID:
1010 21531753.
1011
1012 Vázquez-Diez C, Paim LMG, FitzHarris G. Cell-Size-Independent Spindle Checkpoint
1013 Failure Underlies Chromosome Segregation Error in Mouse Embryos. *Current*
1014 *Biology* [Internet] 2019;**29**:865-873.e3. Cell Press.
1015
1016 Vera-Rodriguez M, Chavez SL, Rubio C, Pera RAR, Simon C. Prediction model for
1017 aneuploidy in early human embryo development revealed by single-cell analysis.
1018 *Nat Commun* [Internet] 2015;**6**:7601. Nature Publishing Group.
1019
1020 Victor AR, Tyndall JC, Brake AJ, Lepkowsky LT, Murphy AE, Griffin DK, McCoy RC,
1021 Barnes FL, Zouves CG, Viotti M. One hundred mosaic embryos transferred
1022 prospectively in a single clinic: exploring when and why they result in healthy
1023 pregnancies. *Fertil Steril* [Internet] 2019;**111**:280–293. Elsevier Inc.
1024
1025 Viotti M, Victor AR, Barnes FL, Zouves CG, Besser AG, Grifo JA, Cheng EH, Lee
1026 MS, Horcajadas JA, Corti L, *et al.* Using outcome data from one thousand
1027 mosaic embryo transfers to formulate an embryo ranking system for clinical use.
1028 *Fertil Steril* 2021;**115**:1212–1224. Elsevier Inc.
1029
1030 Voullaire L, Slater H, Williamson R, Wilton L. Chromosome analysis of blastomeres
1031 from human embryos by using comparative genomic hybridization. *Hum Genet*
1032 [Internet] 2000;**106**:210–217.
1033
1034 Wells D, Delhanty JD. Comprehensive chromosomal analysis of human
1035 preimplantation embryos using whole genome amplification and single cell
1036 comparative genomic hybridization. *Mol Hum Reprod* [Internet] 2000;**6**:1055–
1037 1062.
1038
1039 Williams BR, Prabhu VR, Hunter KE, Glazier CM, Whittaker CA, Housman DE, Amon
1040 A. Aneuploidy affects proliferation and spontaneous immortalization in
1041 mammalian cells. *Science* [Internet] 2008;**322**:703–709. Science.
1042
1043 Yan L, Yang M, Guo H, Yang L, Wu J, Li R, Liu P, Lian Y, Zheng X, Yan J, *et al.*
1044 Single-cell RNA-Seq profiling of human preimplantation embryos and embryonic
1045 stem cells. *Nat Struct Mol Biol* [Internet] 2013;**20**:1131–1139. Nature Publishing
1046 Group.
1047
1048 Yang M, Rito T, Metzger J, Naftaly J, Soman R, Hu J, Albertini DF, Barad DH,
1049 Brivanlou AH, Gleicher N. Depletion of aneuploid cells in human embryos and
1050 gastruloids. *Nat Cell Biol* [Internet] 2021;**23**:314–321. Nature Research.

Zamani Esteki M, Viltrop T, Tšuiko O, Tiirats A, Koel M, Nõukas M, Žilina O, Teearu K, Marjonen H, Kahila H, *et al.* In vitro fertilization does not increase the incidence of de novo copy number alterations in fetal and placental lineages. *Nat Med* 2019;

Zhu J, Tsai HJ, Gordon MR, Li R. Cellular Stress Associated with Aneuploidy. *Dev Cell* [Internet] 2018;**44**:420–431. Cell Press.

1060 **Data availability**

1061 Data are available from the corresponding author upon reasonable request. Source
1062 data files are provided for figures 3 and 4. Raw files are not provided due to GDPR
1063 guidelines concerning human embryo research. Count tables generated from the raw
1064 data files are included in the source data files.

1065 **Acknowledgements**

1066 The authors would like to thank Marleen Carlé from the Center for Medical Genetics
1067 (UZ Brussel) for assisting during the tubing of trophectoderm samples. We thank
1068 Wilfried Cools from the Biostatistics and Medical Informatics Group (VUB) for the
1069 statistical advice and the members of the BRIGHTcore facility (UZ Brussel) for
1070 performing the RNA sequencing. We thank Prof. Rajiv McCoy for the scientific input
1071 and data exchange. This study was funded by the Fonds for Scientific Research in
1072 Flanders -G017218N- (Fonds Wetenschappelijk Onderzoek – Vlaanderen [FWO]).
1073 M.R. and E.C.D.D. are doctoral fellows at the FWO.

1074 **Author contributions**

1075 M.R. carried out all the experiments unless stated otherwise, interpreted and analyzed
1076 the results and co-wrote the manuscript. Y.L. and E.C.D.D. performed the
1077 bioinformatics analysis. Y.G. performed the trophectoderm biopsies. P.V. provided and
1078 supervised the diagnoses of the PGT embryos. G.V. and H.V.D.V. provided the
1079 embryos for this study. K.S. interpreted and supervised the experimental work and co-
1080 wrote the manuscript. C.S. designed, interpreted and supervised the experimental
1081 work and co-wrote the manuscript. All co-authors proofread the manuscript.

1082

Competing interests

The authors declare no competing interests.

1086 **Fig. 1: RNA-sequencing of trophectoderm cells reveals deregulation of DNA**
1087 **damage, p53, cell-cycle, autophagy and apoptosis pathways in chromosomally**
1088 **abnormal human embryos.**

1089 **a**. Human blastocysts 5 or 6 days post-fertilization (dpf) underwent Preimplantation
1090 Genetic Testing (PGT) for monogenic diseases and/or aneuploidy screening, followed
1091 by cryopreservation. Embryos that were not transferred were donated for research
1092 after written informed content. After warming and 2hrs recuperation, euploid and fully
1093 aneuploid research embryos underwent a second TE biopsy for RNA-sequencing. The
1094 remainder of the embryos was live-stained with either CASP3/7 or CASP8 for 30min
1095 and fixed for immunostaining for proteins of interest (see figure 3). **b**. 3dpf human
1096 embryos were warmed and treated with 0.5μM reversine for 24hrs then transferred to
1097 normal culture medium until 5dpf to undergo TE biopsy for RNA-sequencing. After 2hrs
1098 recuperation the embryos were live-stained with CASP8 for 30min and fixed for
1099 immunostaining for proteins of interest (see figure 3). **c**. Unsupervised hierarchical
1100 clustering of all coding genes. Color coding: beige = euploid, red = aneuploid and blue
1101 = reversine-treated. **d**. Comparison between the diagnosis of aneuploid embryos
1102 obtained after PGT (list on the left) and the results obtained after using InferCNV after
1103 RNA-sequencing (plot on the right). **e**,**f**. Volcano plots after differential gene expression
1104 analysis with a cutoff value of $|\log_2$ fold change$| > 1$ and $-\log_{10}$(p-value) < 0.05 for
1105 aneuploid versus euploid (**e**) and reversine versus euploid (**f**). **g**,**h**. Venn diagrams
1106 comparing the upregulated (**g**) and downregulated (**h**) genes in aneuploid versus
1107 reversine treated embryos. **i**,**j**. Supervised plot of pathway analysis using the Molecular
1108 Signatures Database (FDR < 0.05) based on the list of all differentially expressed
1109 genes between aneuploid or reversine versus euploid embryos. Pathways are ranked
1110 based on the total number of genes in overlap of both test sets, ranked from sets with

1111 the highest number of genes in overlap to sets with the lowest. Outputs of the Hallmark
1112 library and C5 ontology gene sets are shown in (**i**) and (**j**), respectively. **k**,**l**. Supervised
1113 plots after Ingenuity Pathway Analysis of upstream regulators with an activation z-
1114 score ≤ -2 and ≥ 2 and a p-value < 0.05 in the aneuploid (**k**) or reversine (**l**) versus
1115 euploid embryos. **m**,**n**. Supervised plots after Ingenuity Pathway Analysis of canonical
1116 pathways in aneuploid (**m**) or reversine (**n**) versus euploid embryos. Pathways are
1117 ranked by p-value from the most to the least significant, those with a p-value < 0.05
1118 and with an activation z-score ≤ -1.5 and ≥ 1.5 were considered as inhibited or
1119 activated, respectively. Significant pathways with an activation z-score between -1.5
1120 and 1.5 were considered as deregulated.

1121

1122 **Fig. 2: Human embryos with the highest number of genes with abnormal copy**
1123 **number show stronger p53 pathway and apoptosis response.**

1124 **a.** Supervised hierarchical clustering of the TOP 500 deregulated genes sorted by p-
1125 value. Color coding: blue = euploid , green = Low dosage and red = High dosage. **b**,**c**.
1126 Volcano plots after differential gene expression analysis with a cutoff value of $|\log_2$ fold
1127 change$|$ > 1 and $-\log_{10}$(p-value) < 0.05 for low dosage versus euploid embryos (**b**) and
1128 high dosage versus euploid embryos (**c**). **d**,**e**, Venn diagrams comparing the
1129 upregulated (**d**) and downregulated (**e**) genes in low dosage versus high dosage
1130 embryos. **f**. Supervised plot of pathway analysis using the Hallmark library of the
1131 Molecular Signatures Database (FDR < 0.05) based on the list of the TOP 500
1132 expressed genes by p-value between low or high dosage versus euploid embryos.
1133 Pathways are ranked based on FDR-q-values of both test sets, the most significant
1134 deregulated pathway ranked from top to least significant pathway. **g**,**h**. Dot plots of the

1135 genes in overlap with the Hallmark p53 pathway (**g**) and Hallmark apoptosis pathway
1136 (**h**) of both low and high dosage embryos sorted by log_2 Fold Change from the highest
1137 to the lowest. Dots with an increased size and a darker blue represent a higher value
1138 of log_2 Fold Change and lower p-value, respectively. **i**, Violin plots with box and whisker
1139 plots of the counts per million mapped reads of a supervised set of 10 genes (from
1140 Supplementary Table 2) that are part of apoptosis (*BAD, BCL2L1, TNFRSF10B*), p53
1141 pathway (*DRAM1, MDM2, CDKN1A/B, PURPL*), growth arrest (*GADD45A*), and DNA-
1142 damage (*DDB2*). *p = 0.027, **p = 0.010, ***p = 0.004, ****p < 0.001 using the
1143 Jonkheere-Terpstra test. Box and whisker plots show median and minimum to
1144 maximum values.

1145 **Fig. 3: Immunostaining reveals increased apoptosis, autophagy, proteotoxic**
1146 **stress and DNA-damage in chromosomally abnormal human embryos.**

1147 **a**,**b**. Same experimental set-up as described in **Fig. 1 a**,**b**, but focused on
1148 immunostaining analysis. **c**, Orthogonal projections after immunostaining of euploid
1149 and aneuploid embryos for DNA (white) and CASP3/7 (green). **d**, Orthogonal
1150 projections after immunostaining of euploid, aneuploid and reversine-treated embryos
1151 for DNA (white) and CASP8 (green). **e**, CASP3/7 mean intensity per cell. Euploid n=13,
1152 Aneuploid n=8 embryos. Mann-Whitney test, *p = 0.0199. **f**, CASP8 mean intensity per
1153 cell. Euploid n=6, Aneuploid n=9, Reversine-treated n=8 embryos. Kruskal-Wallis test,
1154 *p = 0.0394, **p = 0.0085. **g**, Number of nuclei per embryo. Euploid n=19, Aneuploid
1155 n=18, Reversine-treated n=8 embryos. Kruskal-Wallis test, ****p < 0.0001, *p = 0.0305.
1156 **h**, Orthogonal projections after immunostaining of euploid, aneuploid and reversine-
1157 treated embryos for DNA (white), LC3B (turquoise) and HSP70 (magenta). **i**, LC3B
1158 puncta per cell. Euploid n=19, Aneuploid n=22 embryos, Reversine-treated n=8
1159 embryos. Kruskal-Wallis test, *p = 0.0189, **p = 0.0074. **j**, HSP70 mean intensity per

1160 cell. Euploid n=13, Aneuploid n=8, Reversine-treated n=8 embryos. Kruskal-Wallis
1161 test, **p = 0.0077, ***p = 0.0008. **k**, Orthogonal projections after immunostaining of
1162 euploid, aneuploid for DNA (white) and p62 (turquoise). **l**, p62 puncta per cell. Euploid
1163 n=6, Aneuploid n=9 embryos. Mann-Whitney test, **p = 0.0076.

1164 Brightfield pictures were obtained during confocal imaging. All scale bars are 20 µm.
1165 Box and whisker plots show median and whiskers show minimum to maximum values.
1166 Bar plots show mean ± s.d. For all plots each dot represents a single embryo and ns
1167 = not significant.

1168

1169 **Fig. 4: Aneuploid human embryos show less cells in trophectoderm and OCT4-**
1170 **positive cells and impaired second lineage segregation**

1171 **a**, 5 or 6dpf post-PGT-A euploid and fully aneuploid human blastocysts were warmed
1172 and kept for 16hrs in culture to allow for the second lineage segregation. The
1173 blastocysts were live-stained with CASP3/7 for 30min and fixed for immunostaining
1174 proteins of interest. In a first scan we analyzed OCT4 (ICM), CASP3/7 (apoptosis),
1175 LC3B (autophagy) and S15p53 (DNA damage) in both lineages. Embryos were then
1176 re-stained with GATA4 as a marker for PrE. **b,** Orthogonal projections after
1177 immunostaining of euploid, aneuploid for DNA (white) and Serine (S) 15 p53
1178 (turquoise). **c**, Percentage (%) of Serine 15 p53 positive cells per embryo. Euploid n =
1179 3, Aneuploid n = 5. Mann-Whitney test, *p = 0.0357. **d**, Orthogonal projections after
1180 immunostaining of euploid and aneuploid embryos for DNA (white) and OCT4
1181 (magenta). The first aneuploid panel (Trisomy 14 and 16) shows a similar number of
1182 ICM cells compared to the euploid embryo. The second aneuploid panel (Trisomy 14
1183 and 22) shows an embryo without an ICM. **e,f**,**g**, Differences in number of nuclei per

1184 embryo between euploid and aneuploid embryos in the OCT4-negative cells
1185 (trophectoderm) (**e**) **p = 0.0092 , OCT4-positive cells (ICM/EPI), *p = 0.0412 (**f**) and
1186 whole embryo **p = 0.0067 (**g**). Euploid n = 10, Aneuploid n = 14. Student's t-test with
1187 Welch's correction**.** **h**, Orthogonal projections after immunostaining of euploid and
1188 aneuploid embryos for DNA (white), CASP3/7 (green) and OCT4 (magenta). **i**,
1189 Percentage (%) of CASP3/7 positive (+) cells in the trophectoderm lineage (OCT4-
1190 negative cells). Euploid n = 9, Aneuploid n = 14. Student's t-test with Welch's
1191 correction, *p = 0.0453. **j**, CASP3/7 mean intensity per cell of whole embryos. Euploid
1192 n = 9, Aneuploid n = 14. Student's t-test with Welch's correction, *p = 0.0332. **k**,
1193 Orthogonal projections after immunostaining of euploid and aneuploid embryos for
1194 DNA (white), OCT4 (magenta) and GATA4 (green). The first aneuploid panel (trisomy
1195 13 and 15) shows an embryo with presence of a GATA4 positive cell (PrE). The second
1196 aneuploid panel (Trisomy 7 and monosomies 5, 12 and 21) shows an embryo that did
1197 not contain GATA4 positive cells. **l**, Differences in the number of cells per embryo that
1198 were OCT4 positive and either GATA4 negative (red) or positive (green) between
1199 euploid and aneuploid embryos. In case GATA4-positive cells (PrE) were present we
1200 considered the GATA4-negative cells to be epiblast (EPI). All euploid embryos
1201 contained GATA4-positive cells, 7/14 aneuploid embryos had an ICM completely
1202 lacking GATA4-positive cells (Fisher-exact test, p = 0.0188). **m**, Differences in the
1203 PrE/EPI ratio between euploid and aneuploid embryos that had an ICM containing
1204 GATA4-positive cells. Euploid n = 9, Aneuploid n = 7. Note here that one euploid
1205 embryo (#6, **l**) was lost during re-staining for GATA4. Mann-Whitney test, **p = 0.0089.
1206 **n**, Orthogonal projections after immunostaining of euploid and aneuploid embryos for
1207 DNA (white), LC3B (turquoise) and OCT4 (magenta). Yellow circle indicates the ICM.
1208 The first aneuploid panel (Trisomy 1 and 20 and monosomy 18) shows OCT4-positive
1209 cells (ICM/EPI) with low levels of autophagy and, after re-staining for GATA4, without

1210 PrE (right panel, ICM zoom). The second aneuploid panel (Monosomy 14) shows an
1211 embryo with high levels of autophagy in the ICM that contains PrE cells (right panel,
1212 ICM zoom). **o,p,q.** Differences in LC3B puncta per cell between euploid and aneuploid
1213 embryos in the whole embryo,*p = 0.0317 (**o**),(OCT4-negative cells (trophectoderm),*p
1214 = 0.0317 (**p**) and OCT4-positive cells (ICM/EPI) (**q**). Euploid n = 4, Aneuploid n = 5.
1215 Mann-Whitney test. **r**, Violin plots with box plots of OCT4-positive-cells (ICM/EPI) per
1216 embryo (left, ns), OCT4-negative cells (trophectoderm) per embryo (center, *p = 0.043)
1217 and GATA4-positive-cells (PrE) per embryo (right, ****p < 0.001, Jonkheere-Terpstra
1218 test) depending on gene dosage. Euploid (light blue), Low dosage (middle blue) and
1219 High dosage (darkest blue).

1220 Yellow arrows indicate presence of the signal and yellow arrow heads indicate absence
1221 of signal. Brightfield pictures were obtained during confocal imaging. All scale bars are
1222 20 µm. Box and whisker plots show median and minimum to maximum values. Bar
1223 plots show mean ± s.d. For all plots each dot represents a single embryo; ns = not
1224 significant. T = Trisomy, M = Monosomy

1225

1226 **Supplementary Fig. 1: Expanded RNA-sequencing analysis**

1227 **a**, Principal component analysis after RNA-sequencing of euploid (green) versus
1228 aneuploid (red) and reversine (blue) embryos. **b**, InferCNV analysis of individual
1229 euploid samples compared to the reference set. **c**, InferCNV analysis of individual
1230 reversine samples compared to the reference set. **d**, Venn Diagram of overlap between
1231 differentially expressed genes of this study with three studies that analyzed human
1232 embryos that contain euploid and diverse types of aneuploidy from cleavage stage
1233 embryos (Vera-Rodriguez et al. 2015), single cells from 4 and 7 dpf human embryos

1234 from TE, ICM, EPI and PrE lineages (Starostik et al. 2020) and ICM and TE samples
1235 of 5 or 6 dpf embryos containing low- and high levels of mosaicism (Martin *et al.*, 2023).
1236 **e**, Venn Diagram of overlap between differentially expressed genes of this study with
1237 four studies that analyzed specific aneuploidies (Licciardi et al. 2018, Fuchs-Weizman
1238 et al. 2019, Sánchez-Ribas et al. 2019 and Maxwell et al. 2022).

1239

1240 **Supplementary Fig. 2: S15-p53 expression in TE vs OCT4-positive cells (ICM/EPI)**
1241 **and increased micronuclei in aneuploid embryos**

1242 **a**, Orthogonal projections after immunostaining of euploid and aneuploid embryos for
1243 DNA (white), S15p53 (turquoise) and OCT4 (magenta). **b**, Percentages of nuclei
1244 positive for S15p53 per embryo in euploid (n = 3) and aneuploid (n = 4) embryos in the
1245 ICM. **c**, Percentages of nuclei positive for S15p53 per embryo in euploid (n = 3) and
1246 aneuploid (n = 5) embryos in the TE. **d**, Left panel: Orthogonal projections after
1247 immunostaining of euploid and aneuploid embryos for DNA (white) and CASP3/7
1248 (green) showing micronuclei. Yellow box indicates zoomed-in region in the right panel.
1249 Yellow arrows indicate presence of micronuclei and overlap between DNA and
1250 CASP3/7. **e**, Number of micronuclei per cell in euploid and aneuploid whole embryos.
1251 Euploid n = 9, Aneuploid n = 14. Student's t-test with Welch's correction, *p = 0.0115.

1252 Brightfield pictures were obtained during confocal imaging. All scale bars are 20 µm.
1253 Box and plots show median and minimum to maximum values. Bar plots show mean
1254 ± s.d. For all plots each dot represents a single embryo; ns = not significant. ROI =
1255 Region of interest.

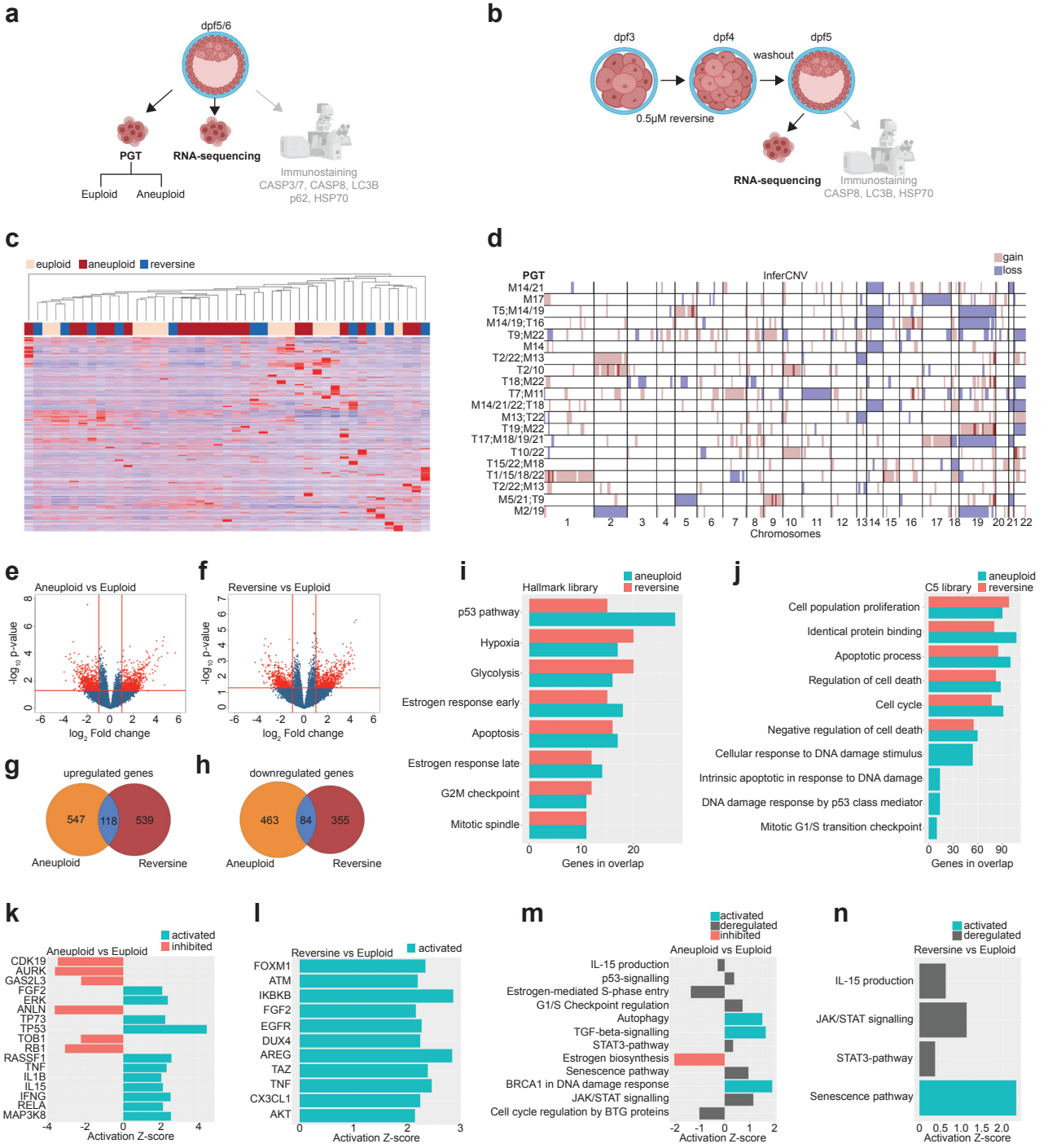
a
dpf5/6
PGT
RNA-sequencing
Euploid
Aneuploid
Immunostaining
CASP3/7, CASP8, LC3B
p62, HSP70
b
dpf3
dpf4
dpf5
washout
0.5μM reversine
RNA-sequencing
Immunostaining
CASP8, LC3B, HSP70
c
euploid
aneuploid
reversine
d
PGT
InferCNV
gain
loss
Chromosomes
e
Aneuploid vs Euploid
-log10 p-value
log2 Fold change
f
Reversine vs Euploid
-log10 p-value
log2 Fold change
g
upregulated genes
547
118
539
Aneuploid
Reversine
h
downregulated genes
463
84
355
Aneuploid
Reversine
i
Hallmark library
aneuploid
reversine
p53 pathway
Hypoxia
Glycolysis
Estrogen response early
Apoptosis
Estrogen response late
G2M checkpoint
Mitotic spindle
Genes in overlap
j
C5 library
aneuploid
reversine
Cell population proliferation
Identical protein binding
Apoptotic process
Regulation of cell death
Cell cycle
Negative regulation of cell death
Cellular response to DNA damage stimulus
Intrinsic apoptotic in response to DNA damage
DNA damage response by p53 class mediator
Mitotic G1/S transition checkpoint
Genes in overlap
k
Aneuploid vs Euploid
activated
inhibited
CDK19
AURK
GAS2L3
FGF2
ERK
ANLN
TP73
TP53
TOB1
RB1
RASSF1
TNF
IL1B
IL15
IFNG
RELA
MAP3K8
Activation Z-score
l
Reversine vs Euploid
activated
FOXM1
ATM
IKBKB
FGF2
EGFR
DUX4
AREG
TAZ
TNF
CX3CL1
AKT
Activation Z-score
m
activated
deregulated
inhibited
Aneuploid vs Euploid
IL-15 production
p53-signalling
Estrogen-mediated S-phase entry
G1/S Checkpoint regulation
Autophagy
TGF-beta-signalling
STAT3-pathway
Estrogen biosynthesis
Senescence pathway
BRCA1 in DNA damage response
JAK/STAT signalling
Cell cycle regulation by BTG proteins
Activation Z-score
n
activated
deregulated
Reversine vs Euploid
IL-15 production
JAK/STAT signalling
STAT3-pathway
Senescence pathway
Activation Z-score

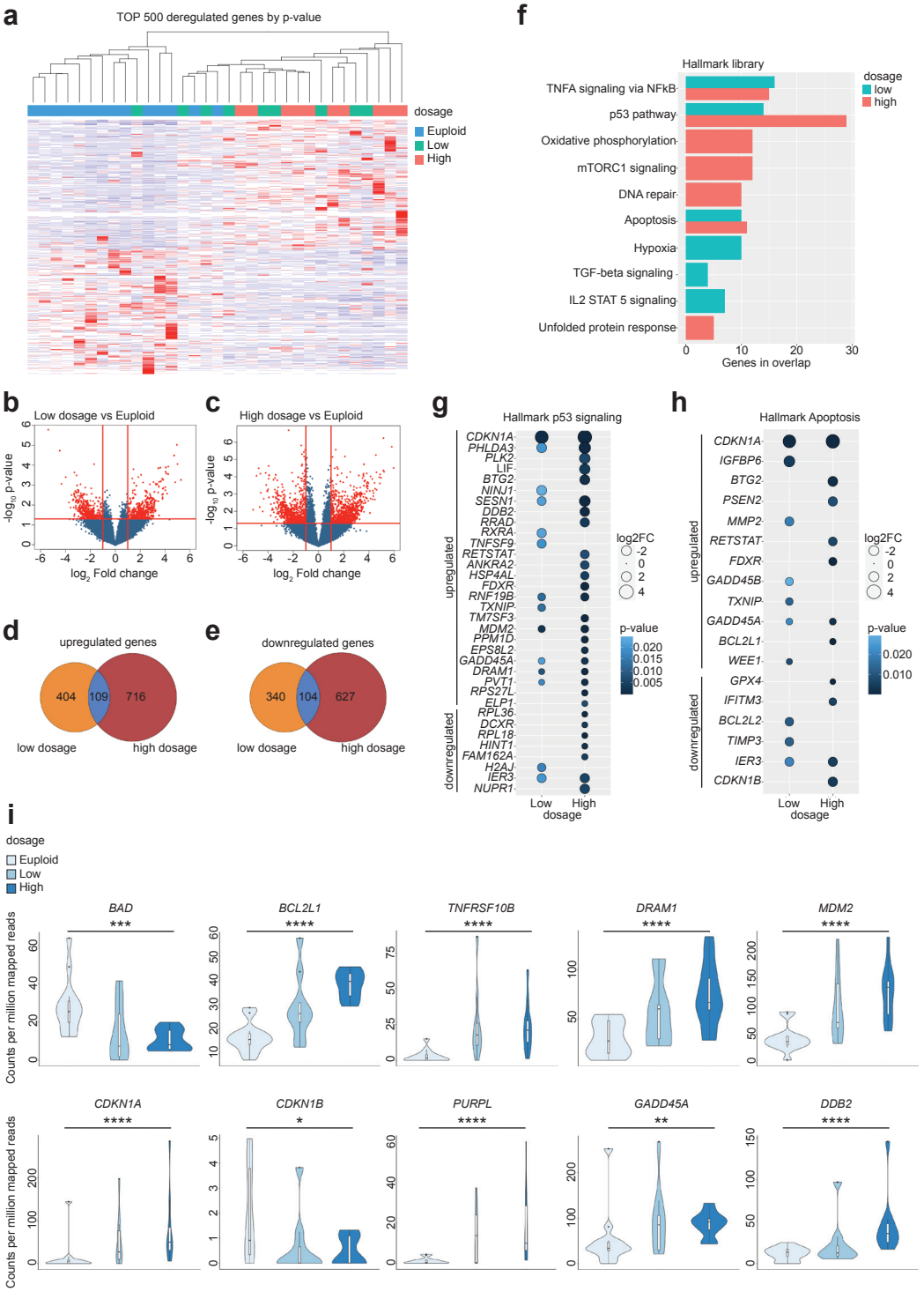
a
TOP 500 deregulated genes by p-value
dosage
Euploid
Low
High
f
Hallmark library
TNFA signaling via NFkB
p53 pathway
Oxidative phosphorylation
mTORC1 signaling
DNA repair
Apoptosis
Hypoxia
TGF-beta signaling
IL2 STAT 5 signaling
Unfolded protein response
Genes in overlap
dosage
low
high
b
Low dosage vs Euploid
-log10 p-value
log2 Fold change
c
High dosage vs Euploid
d
upregulated genes
404
109
716
low dosage
high dosage
e
downregulated genes
340
104
627
low dosage
high dosage
g
Hallmark p53 signaling
upregulated
downregulated
CDKN1A
PHLDA3
PLK2
LIF
BTG2
NINJ1
SESN1
DDB2
RRAD
RXRA
TNFSF9
RETSTAT
ANKRA2
HSP4AL
FDXR
RNF19B
TXNIP
TM7SF3
MDM2
PPM1D
EPS8L2
GADD45A
DRAM1
PVT1
RPS27L
ELP1
RPL36
DCXR
RPL18
HINT1
FAM162A
H2AJ
IER3
NUPR1
Low
High
dosage
log2FC
-2
0
2
4
p-value
0.020
0.015
0.010
0.005
h
Hallmark Apoptosis
upregulated
downregulated
CDKN1A
IGFBP6
BTG2
PSEN2
MMP2
RETSTAT
FDXR
GADD45B
TXNIP
GADD45A
BCL2L1
WEE1
GPX4
IFITM3
BCL2L2
TIMP3
IER3
CDKN1B
Low
High
dosage
log2FC
-2
0
2
4
p-value
0.020
0.010
i
dosage
Euploid
Low
High
BAD
BCL2L1
TNFRSF10B
DRAM1
MDM2
CDKN1A
CDKN1B
PURPL
GADD45A
DDB2
Counts per million mapped reads

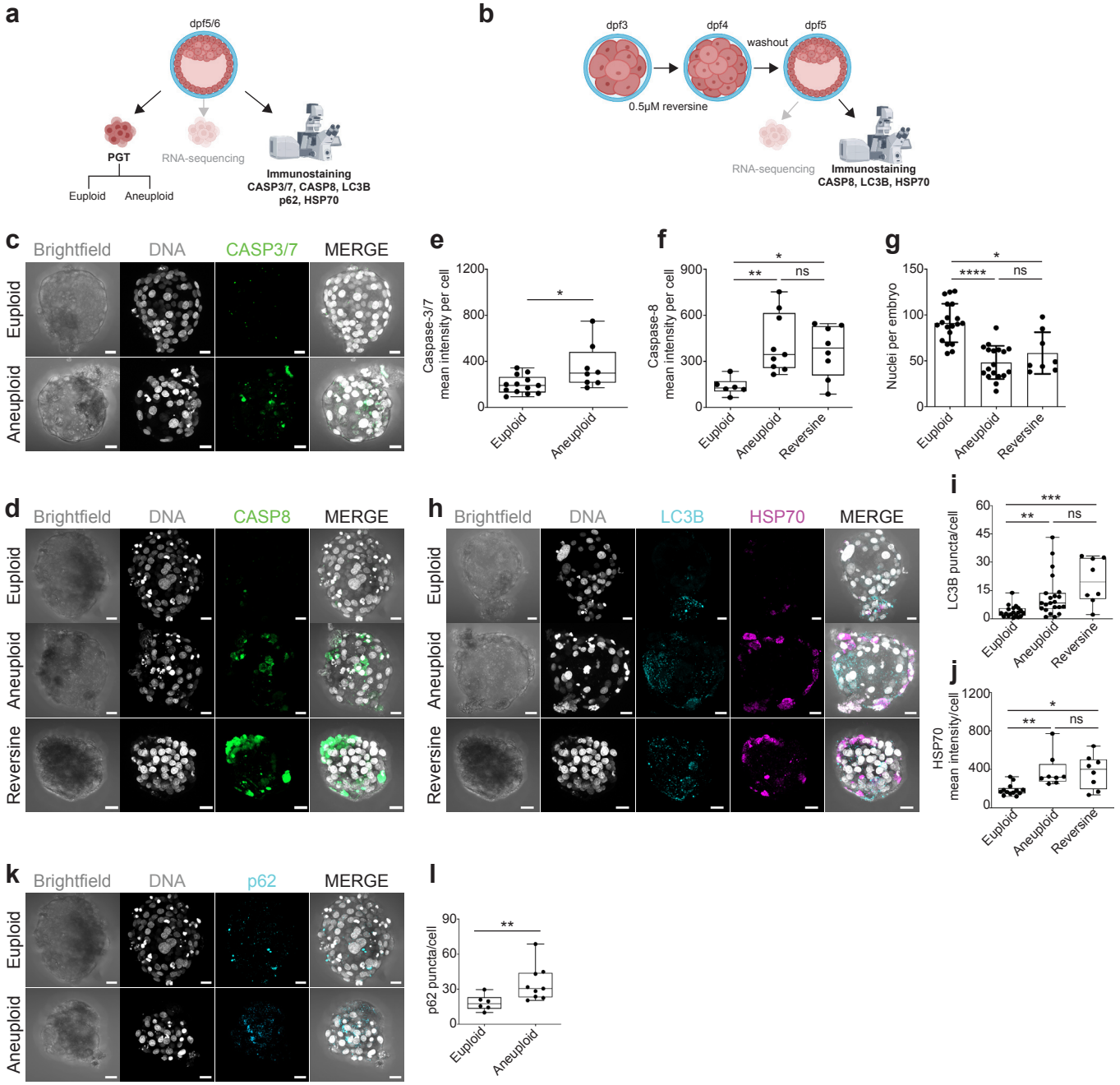
a
dpf5/6
PGT
RNA-sequencing
Euploid
Aneuploid
Immunostaining
CASP3/7, CASP8, LC3B
p62, HSP70
b
dpf3
dpf4
dpf5
washout
0.5μM reversine
RNA-sequencing
Immunostaining
CASP8, LC3B, HSP70
c
Brightfield
DNA
CASP3/7
MERGE
Euploid
Aneuploid
e
Caspase-3/7
mean intensity per cell
Euploid
Aneuploid
f
Caspase-8
mean intensity per cell
Euploid
Aneuploid
Reversine
g
Nuclei per embryo
Euploid
Aneuploid
Reversine
d
Brightfield
DNA
CASP8
MERGE
Euploid
Aneuploid
Reversine
h
Brightfield
DNA
LC3B
HSP70
MERGE
Euploid
Aneuploid
Reversine
i
LC3B puncta/cell
Euploid
Aneuploid
Reversine
j
HSP70
mean intensity/cell
Euploid
Aneuploid
Reversine
k
Brightfield
DNA
p62
MERGE
Euploid
Aneuploid
l
p62 puncta/cell
Euploid
Aneuploid

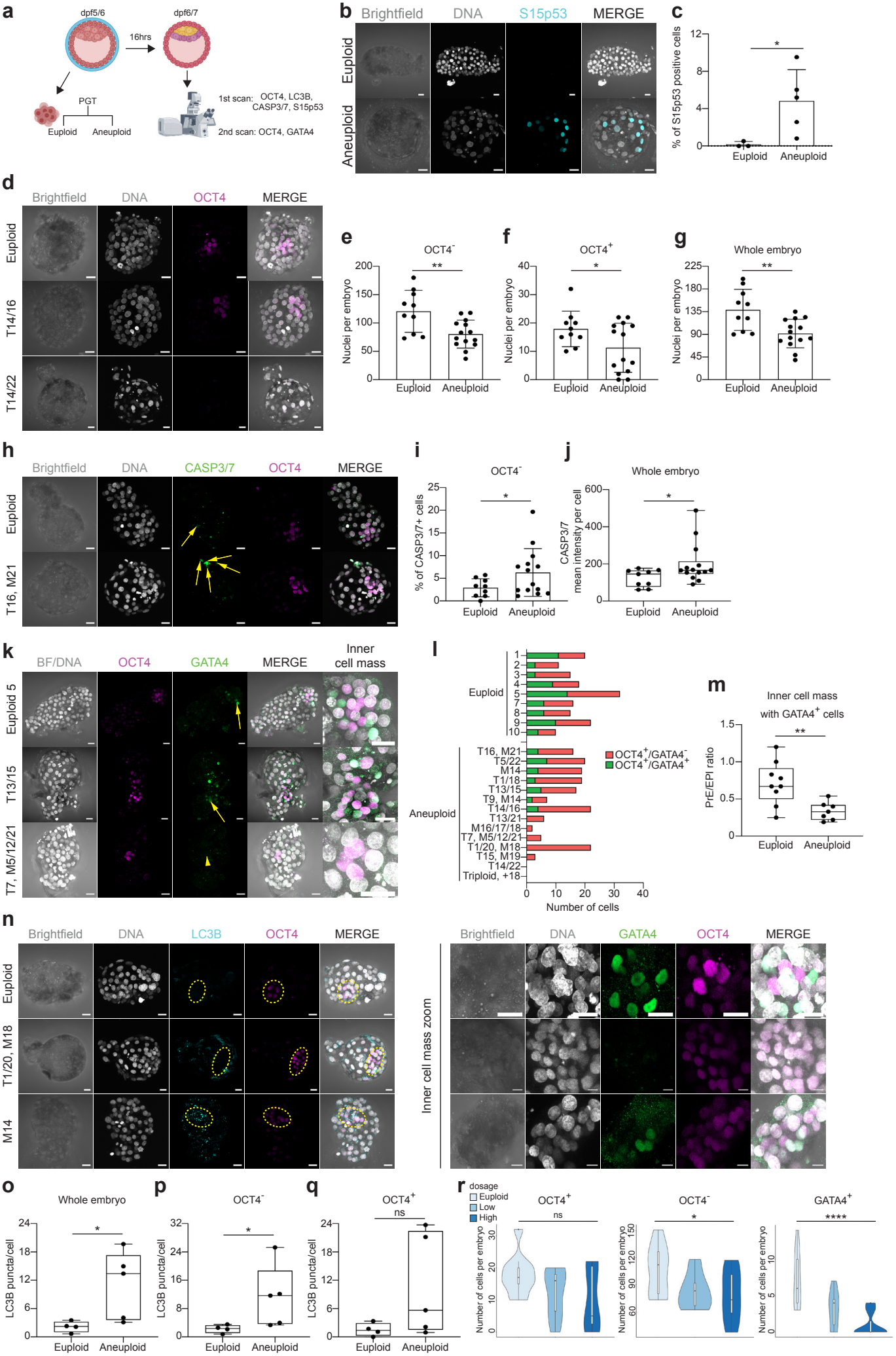
a
dpf5/6
16hrs
dpf6/7
PGT
Euploid
Aneuploid
1st scan: OCT4, LC3B, CASP3/7, S15p53
2nd scan: OCT4, GATA4
b
Brightfield
DNA
S15p53
MERGE
Euploid
Aneuploid
c
% of S15p53 positive cells
Euploid
Aneuploid
d
Brightfield
DNA
OCT4
MERGE
Euploid
T14/16
T14/22
e
OCT4-
Nuclei per embryo
Euploid
Aneuploid
f
OCT4+
Nuclei per embryo
Euploid
Aneuploid
g
Whole embryo
Nuclei per embryo
Euploid
Aneuploid
h
Brightfield
DNA
CASP3/7
OCT4
MERGE
Euploid
T16, M21
i
OCT4-
% of CASP3/7+ cells
Euploid
Aneuploid
j
Whole embryo
CASP3/7 mean intensity per cell
Euploid
Aneuploid
k
BF/DNA
OCT4
GATA4
MERGE
Inner cell mass
Euploid 5
T13/15
T7, M5/12/21
l
Euploid
Aneuploid
T16, M21
T5/22
M14
T1/18
T13/15
T9, M14
T14/16
T13/21
M16/17/18
T7, M5/12/21
T1/20, M18
T15, M19
T14/22
Triploid, +18
OCT4+/GATA4-
OCT4+/GATA4+
Number of cells
m
Inner cell mass with GATA4+ cells
PrE/EPI ratio
Euploid
Aneuploid
n
Brightfield
DNA
LC3B
OCT4
MERGE
Euploid
T1/20, M18
M14
Inner cell mass zoom
GATA4
o
Whole embryo
LC3B puncta/cell
Euploid
Aneuploid
p
OCT4-
LC3B puncta/cell
Euploid
Aneuploid
q
OCT4+
ns
LC3B puncta/cell
Euploid
Aneuploid
r
dosage
Euploid
Low
High
OCT4+
ns
OCT4-
GATA4+
Number of cells per embryo

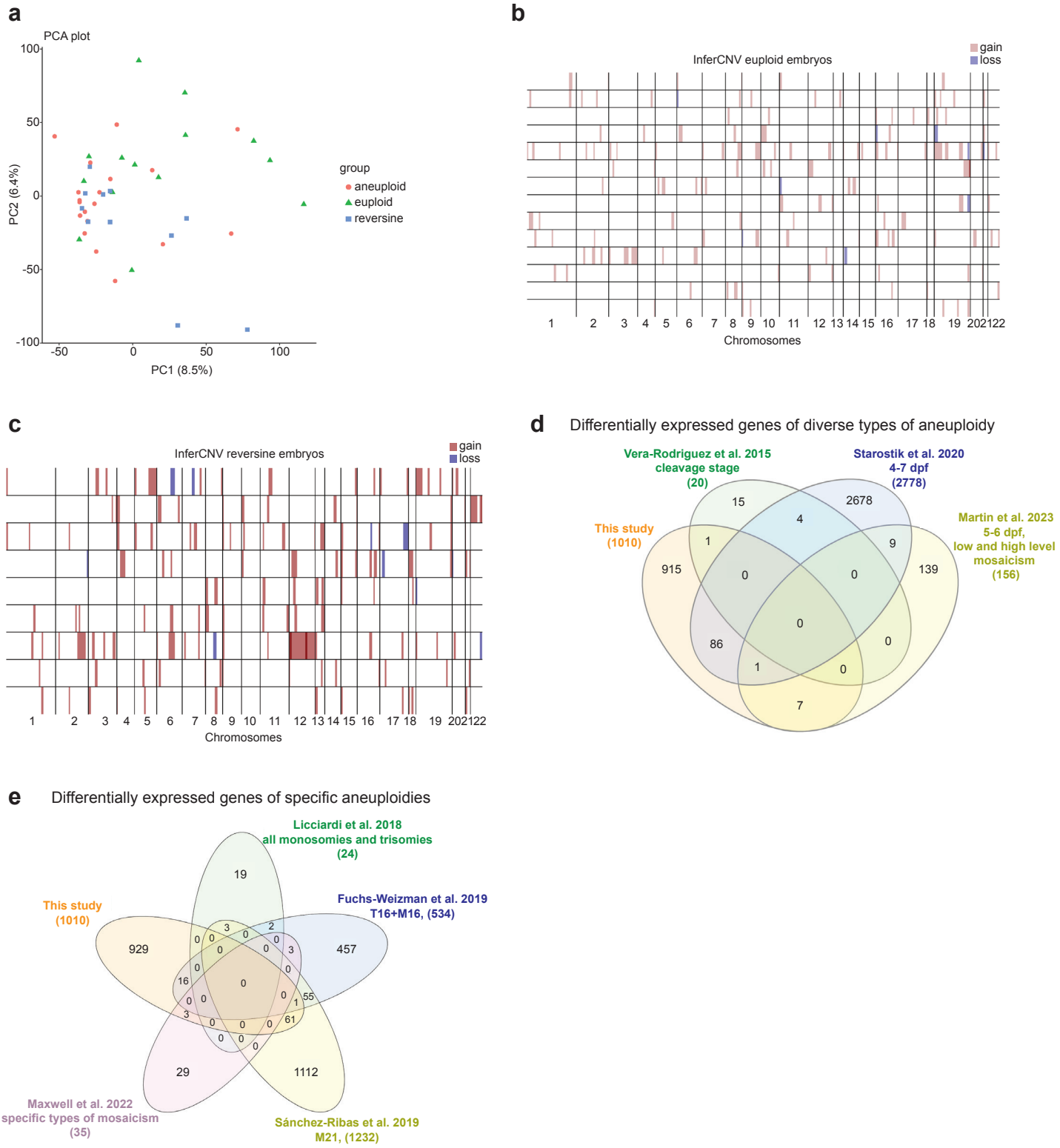
a
PCA plot
PC2 (6.4%)
PC1 (8.5%)
group
aneuploid
euploid
reversine
b
InferCNV euploid embryos
gain
loss
Chromosomes
c
InferCNV reversine embryos
gain
loss
Chromosomes
d
Differentially expressed genes of diverse types of aneuploidy
Vera-Rodriguez et al. 2015
cleavage stage
(20)
Starostik et al. 2020
4-7 dpf
(2778)
This study
(1010)
Martin et al. 2023
5-6 dpf,
low and high level
mosaicism
(156)
e
Differentially expressed genes of specific aneuploidies
Licciardi et al. 2018
all monosomies and trisomies
(24)
This study
(1010)
Fuchs-Weizman et al. 2019
T16+M16, (534)
Maxwell et al. 2022
specific types of mosaicism
(35)
Sánchez-Ribas et al. 2019
M21, (1232)

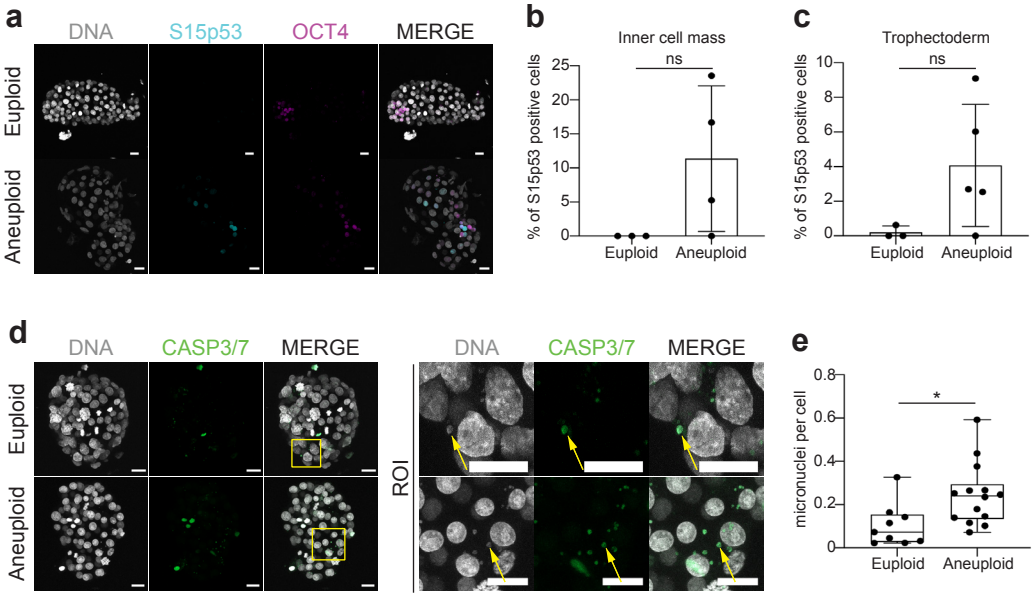
a
DNA
S15p53
OCT4
MERGE
Euploid
Aneuploid
b
Inner cell mass
ns
% of S15p53 positive cells
25
20
15
10
5
0
Euploid
Aneuploid
c
Trophectoderm
ns
% of S15p53 positive cells
10
8
6
4
2
0
Euploid
Aneuploid
d
DNA
CASP3/7
MERGE
Euploid
Aneuploid
ROI
DNA
CASP3/7
MERGE
e
micronuclei per cell
0.8
0.6
0.4
0.2
0
*
Euploid
Aneuploid